

# Leiomodin-3 dysfunction results in thin filament disorganization and nemaline myopathy

Michaela Yuen,<sup>1,2</sup> Sarah A. Sandaradura,<sup>1,2</sup> James J. Dowling,<sup>3,4</sup> Alla S. Kostyukova,<sup>5</sup> Natalia Moroz,<sup>5</sup> Kate G. Quinlan,<sup>1,2</sup> Vilma-Lotta Lehtokari,<sup>6</sup> Gianina Ravenscroft,<sup>7</sup> Emily J. Todd,<sup>7</sup> Ozge Ceyhan-Birsoy,<sup>8</sup> David S. Gokhin,<sup>9</sup> Jérôme Maluenda,<sup>10</sup> Monkol Lek,<sup>11,12</sup> Flora Nolent,<sup>10</sup> Christopher T. Pappas,<sup>13</sup> Stefanie M. Novak,<sup>13</sup> Adele D'Amico,<sup>14</sup> Edoardo Malfatti,<sup>15</sup> Brett P. Thomas,<sup>11,12</sup> Stacey B. Gabriel,<sup>12</sup> Namrata Gupta,<sup>12</sup> Mark J. Daly,<sup>11,12</sup> Biljana Ilkovski,<sup>1</sup> Peter J. Houweling,<sup>1,2,16</sup> Ann E. Davidson,<sup>3,4</sup> Lindsay C. Swanson,<sup>8</sup> Catherine A. Brownstein,<sup>8</sup> Vandana A. Gupta,<sup>8</sup> Livija Medne,<sup>17</sup> Patrick Shannon,<sup>18</sup> Nicole Martin,<sup>19</sup> David P. Bick,<sup>20</sup> Anders Flisberg,<sup>21</sup> Eva Holmberg,<sup>22</sup> Peter Van den Bergh,<sup>23</sup> Pablo Lapunzina,<sup>24,25</sup> Leigh B. Waddell,<sup>1,2</sup> Darcée D. Sloboda,<sup>26</sup> Enrico Bertini,<sup>14</sup> David Chitayat,<sup>19,27</sup> William R. Telfer,<sup>3</sup> Annie Laquerrière,<sup>28</sup> Carol C. Gregorio,<sup>13</sup> Coen A.C. Ottenheijm,<sup>29</sup> Carsten G. Bönnemann,<sup>30</sup> Katarina Pelin,<sup>31</sup> Alan H. Beggs,<sup>8</sup> Yukiko K. Hayashi,<sup>32,33</sup> Norma B. Romero,<sup>15</sup> Nigel G. Laing,<sup>7</sup> Ichizo Nishino,<sup>33</sup> Carina Wallgren-Pettersson,<sup>6</sup> Judith Melki,<sup>10,34</sup> Velia M. Fowler,<sup>9</sup> Daniel G. MacArthur,<sup>11,12</sup> Kathryn N. North,<sup>1,16,35</sup> and Nigel F. Clarke<sup>1,2</sup>

<sup>1</sup>Institute for Neuroscience and Muscle Research, The Children's Hospital at Westmead, Sydney, New South Wales, Australia. <sup>2</sup>Discipline of Paediatrics and Child Health, University of Sydney, Sydney, New South Wales, Australia. <sup>3</sup>Departments of Pediatrics and Neurology, University of Michigan Medical Center, Ann Arbor, Michigan, USA. <sup>4</sup>Division of Neurology and Program of Genetics and Genome Biology, Hospital for Sick Children, Toronto, Ontario, Canada. <sup>5</sup>The Gene and Linda Voiland School of Chemical Engineering and Bioengineering, Washington State University, Pullman, Washington, USA. <sup>6</sup>Folkhälsan Institute of Genetics and Department of Medical Genetics, University of Helsinki, Haartman Institute, Biomedicum Helsinki, Helsinki, Finland. <sup>7</sup>Western Australia Institute for Medical Research and Centre for Medical Research, University of Western Australia, Nedlands, Western Australia, Australia. <sup>8</sup>Division of Genetics and Genomics, The Manton Centre for Orphan Disease Research, Boston Children's Hospital, Harvard Medical School, Boston, Massachusetts, USA. <sup>9</sup>Department of Cell and Molecular Biology, The Scripps Research Institute, La Jolla, California, USA. <sup>10</sup>Unité Mixte de recherche 788, Inserm and University Paris, Le Kremlin-Bicêtre, France. <sup>11</sup>Analytic and Translational Genetics Unit, Massachusetts General Hospital, Boston, Massachusetts, USA. <sup>12</sup>Broad Institute of Harvard and Massachusetts Institute of Technology, Cambridge, Massachusetts, USA. <sup>13</sup>Department of Cellular and Molecular Medicine, University of Arizona, Tucson, Arizona, USA. <sup>14</sup>Laboratory of Molecular Medicine for Neuromuscular and Neurodegenerative Diseases, Bambino Gesù Children's Hospital, Rome, Italy. <sup>15</sup>Neuromuscular Morphology Unit, Institute of Myology, Groupe Hospitalier Universitaire La Pitié-Salpêtrière, Paris, France. <sup>16</sup>Murdoch Children's Research Institute, The Royal Children's Hospital, Parkville, Victoria, Australia. <sup>17</sup>Divisions of Human Genetics and Neurology, Children's Hospital of Philadelphia, Philadelphia, Pennsylvania, USA. <sup>18</sup>Department of Pathology and Laboratory Medicine, Mount Sinai Hospital, Toronto, Ontario, Canada. <sup>19</sup>The Prenatal Diagnosis and Medical Genetics Program, Department of Obstetrics and Gynaecology, Mount Sinai Hospital, University of Toronto, Toronto, Ontario, Canada. <sup>20</sup>Section of Genetics, Department of Pediatrics and Human and Molecular Genetics Center, Medical College of Wisconsin, Milwaukee, Wisconsin, USA. <sup>21</sup>Department of Neonatology and <sup>22</sup>Department of Clinical Genetics, Sahlgrenska University Hospital, Göteborg, Sweden. <sup>23</sup>Neuromuscular Reference Centre, University Hospitals Saint-Luc, Brussels, Belgium. <sup>24</sup>Instituto de Genética Médica y Molecular, Instituto de Investigación Sanitaria del Hospital Universitario La Paz, Madrid, Spain. <sup>25</sup>Universidad Autónoma de Madrid and Centro de Investigación Biomedica en Red de Enfermedades Raras, Instituto de Salud Carlos III, Madrid, Spain. <sup>26</sup>Department of Biomedical Engineering, University of Michigan, Ann Arbor, Michigan, USA. <sup>27</sup>Division of Clinical and Medical Genetics, Department of Paediatrics, The Hospital for Sick Children, University of Toronto, Toronto, Ontario, Canada. <sup>28</sup>Pathology Laboratory and NeoVasc Region-Inserm Team ERI28, University of Rouen, Rouen, France. <sup>29</sup>Department of Physiology, Institute for Cardiovascular Research, VU University Medical Center, Amsterdam, The Netherlands. <sup>30</sup>Neuromuscular and Neurogenetic Disorders of Childhood Section, National Institute of Neurological Disorders and Stroke/NIH, Bethesda, Maryland, USA. <sup>31</sup>Department of Biosciences, University of Helsinki, Helsinki, Finland. <sup>32</sup>Department of Neurophysiology, Tokyo Medical University, Tokyo, Japan. <sup>33</sup>Department of Neuromuscular Research, National Institute of Neuroscience, National Center of Neurology and Psychiatry, Tokyo, Japan. <sup>34</sup>Unité de Génétique Médicale, Centre Hospitalier Sud Francilien, Corbeil Essonnes, France. <sup>35</sup>Department of Paediatrics, University of Melbourne, Victoria, Australia.

**Nemaline myopathy (NM) is a genetic muscle disorder characterized by muscle dysfunction and electron-dense protein accumulations (nemaline bodies) in myofibers. Pathogenic mutations have been described in 9 genes to date, but the genetic basis remains unknown in many cases. Here, using an approach that combined whole-exome sequencing (WES) and Sanger sequencing, we identified homozygous or compound heterozygous variants in *LMOD3* in 21 patients from 14 families with severe, usually lethal, NM. *LMOD3* encodes leiomodin-3 (LMOD3), a 65-kDa protein expressed in skeletal and cardiac muscle. LMOD3 was expressed from early stages of muscle differentiation; localized to actin thin filaments, with enrichment near the pointed ends; and had strong actin filament-nucleating activity. Loss of LMOD3 in patient muscle resulted in shortening and disorganization of thin filaments. Knockdown of *lmod3* in zebrafish replicated NM-associated functional and pathological phenotypes. Together, these findings indicate that mutations in the gene encoding LMOD3 underlie congenital myopathy and demonstrate that LMOD3 is essential for the organization of sarcomeric thin filaments in skeletal muscle.**

**Authorship note:** Michaela Yuen and Sarah A. Sandaradura contributed equally to this work. Kathryn N. North and Nigel F. Clarke contributed equally to this work and are co-senior authors.

**Conflict of interest:** The authors have declared that no conflict of interest exists.

**Submitted:** January 30, 2014; **Accepted:** August 19, 2014.

**Reference information:** *J Clin Invest.* doi:10.1172/JCI75199.

## Introduction

Nemaline myopathy (NM) is a common form of congenital myopathy, affecting approximately 1 in 50,000 individuals, and is defined by the presence of nonprogressive generalized muscle weakness and numerous electron-dense protein inclusions (nemaline bodies or rods) in skeletal myofibers (1). The most severely affected

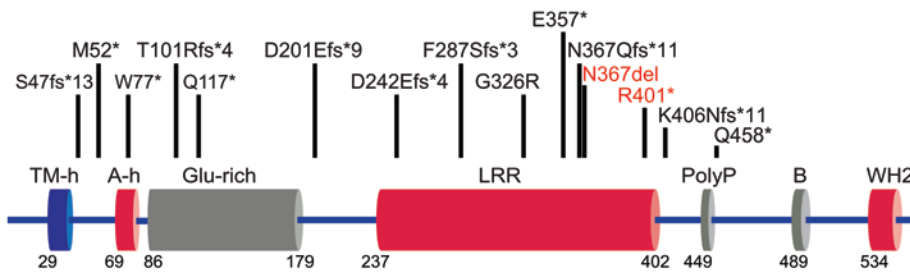


**Figure 1. LMOD3 mutations in patients with LMOD3-NM.** Schematic of LMOD3 (NP\_938012) showing domain organization, with mutation positions indicated. Protein structure information was obtained from Chereau et al. (10), UniProt (<http://www.uniprot.org/>), and InterProScan 4 (37). LMOD3 contains 3 actin-binding domains (red) (actin-binding helix [A-h], residues 69–79; leucine-rich repeat domain [LLR], residues 237–402; Wiskott-Aldrich-syndrome protein homology 2 domain [WH2], residues 534–553) and 1 TM-binding helix (TM-h, residues 29–40). The functions of the proline-rich region (PolyP, residues 449–457), Glu-rich region (residues 86–179), and basic region (B, residues 489–498) are unknown. Mutations indicated in red font are associated with expression of mutant protein in Western blot studies (see Figure 2).

children with NM die in the neonatal period from respiratory insufficiency. Less severely affected patients often have difficulties walking and swallowing and require nocturnal respiratory support. Nine genes have been linked to NM to date; *NEB*, *ACTA1*, *TPM3*, *TPM2*, *CFL2*, and *TNNT1* all encode components of the sarcomeric thin filament in skeletal muscle, while *KBTBD13*, *KLHL40*, and *KLHL41*, which belong to the BTB-BACK-kelch (BBK) protein family, are thought to be involved in ubiquitination and protein degradation (2, 3). However many patients with NM do not have identifiable mutations in these genes, suggesting there is further genetic heterogeneity.

Whole-exome sequencing (WES) and other approaches that use next-generation sequencing technology have revolutionized gene discovery by allowing rapid, cost-effective screening of large regions of the genome for potentially pathogenic variants. To identify further genetic causes of NM, we used WES on 2 multiplex NM families who lacked a genetic diagnosis after standard investigations.

## Results

*Mutations in LMOD3 are a new genetic cause for NM and most mutations result in complete loss of leiomodiodin-3 protein expression.* WES in 2 unrelated families with NM identified likely mutations in *LMOD3*, which encodes leiomodiodin-3 (*LMOD3*). In the consanguineous family 1, a homozygous frameshift variant in *LMOD3* was identified in both affected siblings. In nonconsanguineous family 14, WES identified previously unreported compound heterozygous *LMOD3* variants in both affected children. In both families, segregation was consistent with autosomal recessive inheritance.

Genetic screening of the 3 coding exons of *LMOD3* by Sanger sequencing, WES, or whole-genome sequencing in over 540 additional genetically unresolved probands with NM identified likely pathogenic variants in 17 patients from 12 additional families (Figure 1 and Table 1). Segregation studies were consistent with autosomal recessive inheritance. Most other common genetic causes of NM had been excluded previously in patients in whom *LMOD3* variants were identified (Supplemental Table 1; supplemental material available online with this article; doi:10.1172/JCI75199DS1). *LMOD3* variants were distributed throughout the gene and most

were nonsense or frameshift mutations that are predicted to truncate *LMOD3* (Figure 1 and Table 1). A heterozygous missense variant in *LMOD3*, c.976G>C (p.G326R), was identified in probands from 2 unrelated families (families 8 and 10) in association with different heterozygous truncating mutations (Figure 1 and Table 1). This variant was not present in the National Heart, Lung, and Blood Institute Exome Sequencing Project or the 1000 Genomes databases, which contain exome sequence data from a large number of individuals without muscle disorders, suggesting that the c.976G>C variant is very rare in the general

population and is very unlikely to be associated with severe NM in families 8 and 10 by chance alone. Amino acid G326 is conserved in the *LMOD1*, *LMOD2*, and *LMOD3* and *TMOD1*, *TMOD2*, and *TMOD3* proteins and is located within the leucine-rich repeat domain of *LMOD3* (Figure 1), which is predicted to bind actin. In silico prediction of the functional consequences of this variant was supportive of pathogenicity (PolyPhen-2 score 1.00 = probably damaging, SIFT score 0 = damaging). Together, these data support the hypothesis that the c.976G>C (p.G326R) variant disrupts gene function and is pathogenic.

Although tissue was not available from affected individuals in all families, Western blotting confirmed that many mutations result in no detectable *LMOD3* protein in muscle, with the exception of patient 14a, in whom protein expression from both mutant alleles was demonstrated (Figure 2A and Table 1). To confirm these results, we analyzed primary myoblast cell lines and/or fibroblast cell lines (transformed into myogenic cells using MyoD transduction; refs. 4, 5) derived from the probands of families 12 and 14. Western blot analysis confirmed the absence of *LMOD3* expression in myotubes from family 12 and the expression of both mutant forms of *LMOD3* in myotubes from patient 14a (Figure 2B). In addition, we confirmed that the polyclonal *LMOD3* Ab we used was able to detect N-terminal protein fragments 51–amino acids long (Supplemental Figure 1), corresponding to the shortest predicted *LMOD3* truncation in our cohort.

*NM patients with LMOD3 mutations typically have severe congenital NM and distinctive nemaline body morphology on electron microscopy.* NM patients with *LMOD3* mutations (*LMOD3*-NM) presented with severe congenital NM in 90% of cases (13 of 14 families) (Table 2). Antenatal manifestations included polyhydramnios (62% of patients), decreased or absent fetal movements (48% of patients), and joint contractures (often multiple, 48% of patients). Thirty-five percent of patients were born prematurely. All patients had severe generalized hypotonia and weakness at birth, respiratory insufficiency, feeding difficulties, and bulbar weakness (Figure 3, A and B, and Table 2). Twenty-nine percent of patients had ophthalmoplegia, which is uncommon in other genetic forms of NM. Most patients died in the neonatal period from respiratory failure. No cardiac abnormalities were reported. Two sisters from

**Table 1. *LMOD3* variants and protein expression**

Patient ID	<i>LMOD3</i> genotype <sup>a</sup>	Protein expression <sup>b</sup>
1a	hom c.138dupC, p.S47fs*13	p.S47fs*13 (6.6 kDa), no expression
1b	hom c.138dupC, p.S47fs*13	p.S47fs*13 (6.6 kDa), N/D
2	hom c.138dupC, p.S47fs*13	p.S47fs*13 (6.6 kDa), N/D
3	hom c.154delA, p.M52*	3a and 3b - p.M52* (5.7 kDa), N/D
4	hom c.231G>A, p.W77*	p.W77*(8.7 kDa), no expression
5	het c.300_304delGACTC, p.T101Rfs*4 het c.601_602delGGA, p.D201Efs*9	p.T101Rfs*4 (12 kDa), no expression p.D201Efs*9 (24 kDa), no expression
6	hom c.349C>T, p.Q117*	p.Q117*(13.6 kDa), inconclusive
7	het c.349C>T, p.Q117* het c.1218delA, p.K406Nfs*11	p.Q117* (13.6 kDa), inconclusive p.K406Nfs*11 (48.2 kDa), inconclusive
8	het c.723_733del, p.D242Efs*4 het c.976G>C, p.G326R	p.G326R p.D242Efs*4 (28.3 kDa), N/D
9	hom c.860delT, p.F287Sfs*3	p.F287Sfs*3 (33 kDa), no expression
10	het c.976G>C, p.G326R het c.1372C>T, p.Q458*	p.Q458* (52.9 kDa), N/D p.G326R
11a	hom c.1069G>T, p.E357*	p.E357* (41.1 kDa), N/D
11b	hom c.1069G>T, p.E357*	p.E357* (41.1 kDa), N/D
12a <sup>c</sup>	hom c.1099_1100delAA, p.N367Qfs*11	p.N367Qfs*11 (43 kDa), no expression
12b	hom c.1099_1100delAA, p.N367Qfs*11	p.N367Qfs*11 (43 kDa), N/D
12c	hom c.1099_1100delAA, p.N367Qfs*11	p.N367Qfs*11 (43 kDa), no expression
13a	hom c.1099_1100delAA, p.N367Qfs*11	p.N367Qfs*11 (43 kDa), N/D
13b	hom c.1099_1100delAA, p.N367Qfs*11	p.N367Qfs*11 (43 kDa), N/D
14a	het c.1100_1102delACA, p.N367del het c.1201C>T, p.R401*	p.R401* (48 kDa), expressed p.N367del (64.8 kDa), expressed
14b	het c.1100_1102delACA, p.N367del het c.1201C>T, p.R401*	p.N367del, N/D p.R401*, N/D

<sup>a</sup>Numbering of the nucleotide and protein changes is relative to NM\_198271.3 (gene) and NP\_938012 (protein). <sup>b</sup>Full-length *LMOD3* protein is 560-amino acids long and has a predicted molecular weight of 64.9 kDa. Molecular weight predictions were performed using ExPASy ([http://web.expasy.org/compute\\_pi/](http://web.expasy.org/compute_pi/)). The presence or absence of protein expression was assessed by Western blot analysis. <sup>c</sup>Corresponds to BOS-1120. Hom, homozygous; het, heterozygous; N/D, not determined (no muscle was available for analysis); inconclusive, biopsy contained only small amounts of muscle tissue, and the presence or absence of mutant *LMOD3* expression could not be determined conclusively.

family 14 are the only known surviving patients, currently aged 10 and 4 years. Lower limb muscle MRI in patient 14a demonstrated widespread atrophy and fatty infiltration of thigh and lower leg muscles, with relative sparing of some muscles, including vastus lateralis, gracilis, semimembranosus, semitendinosus, and extensor digitorum longus (Supplemental Figure 2).

Light microscopy images of skeletal muscle biopsies were available from 11 patients, and electron microscopy (EM) images were available from 6 patients. Histological assessment revealed nemaline bodies and atrophic myofibers in all *LaMOD3*-NM muscle biopsies. Interstitial connective tissue was increased in all biopsies and had almost completely replaced myofibers in 5 of 11 biopsies (Figure 3D). On EM images, many nemaline bodies resembled short thickened Z-discs (seen in all 6 patients for whom EM images were available; Figure 3, G and H), often in doublets interconnected by filaments (present in 4 of 6 patient biopsies; Figure 3I). Some nemaline bodies were surrounded by a short thin filament “fringe” 60–220 nm in length (Figure 3, I and J; present in 3 of 6 patient biopsies).

*A zebrafish model of LMOD3-NM recapitulates the human phenotype.* As further confirmation that loss of *LMOD3* leads to skeletal muscle disease, we developed a zebrafish knockdown model of *LMOD3*-NM (Figure 4). Coinjection of 2 morpholinos targeting different splice sites of the zebrafish *lmod3* gene achieved a knockdown of gene transcripts and markedly reduced *Lmod3* protein expression in injected zebrafish (Figure 4B). *lmod3* knockdown fish larvae (*lmod3* MO) assessed 3 days after fertilization had short bodies, bent tails, and reduced tail birefringence, consistent with abnormal skeletal muscle organization, which was also observed on EM images (Figure 4A and Supplemental Figure 3). *lmod3* MO also had reduced trunk muscle cross-sectional areas (*lmod3* MO:  $0.021 \pm 0.003$  mm<sup>2</sup> [ $n = 5$ ], control morphants [control MO]:  $0.028 \pm 0.002$  mm<sup>2</sup> [ $n = 5$ ],  $P = 0.003$ , 2-tailed unpaired  $t$  test). Immunostaining showed aberrant accumulations of the Z-disc protein  $\alpha$ -actinin, a major component of nemaline bodies (Figure 4, C and D). Knockdown embryos also demonstrated abnormal motor function, with reduced spontaneous coiling (*lmod3* MO:  $0.7 \pm 0.2$  coils per 15 seconds [ $n = 68$ ], control MO:  $5.7 \pm 0.5$  coils per 15 seconds [ $n = 76$ ],  $P < 0.0001$ ; Figure 4E) and diminished touch-evoked escape responses (*lmod3* MO: average  $1.0 \pm 0.1$  [ $n = 55$ ], control MO: average  $2.6 \pm 0.1$  [ $n = 134$ ],  $P < 0.0001$ ; Figure 4F). Trunk muscles of *lmod3* MO (3 days after fertilization) generated less force (*lmod3* MO:  $4 \pm 3$  mN/mm<sup>2</sup> [ $n = 5$ ], control MO:  $26 \pm 6$  mN/mm<sup>2</sup> [ $n = 5$ ],  $P < 0.0001$ ; Figure 4G). Forces were normalized to cross-sectional area to confirm that weakness of *lmod3* MO was not solely due to reduced *lmod3* MO muscle size.

*LMOD3 is expressed in skeletal muscle throughout life and localizes to the actin thin filament.* The leiomodins are members of the tropomodulin protein family, and 3 leiomodin genes have been identified so far: *LMOD1*, *LMOD2*, and *LMOD3*. *LMOD1* is expressed predominantly in smooth muscle, while *LMOD2* and *LMOD3* are mainly found in skeletal and cardiac muscle (6, 7). Until now, *LMOD3* has been little studied, and its roles in skeletal and cardiac muscle have been unclear.

We performed protein studies in healthy muscle to characterize *LMOD3* expression and localization. Western blot analysis on control human heart and skeletal muscle biopsies demonstrated that *LMOD3* was expressed at higher levels in skeletal muscle than in cardiac muscle, while the situation was reversed for *LMOD2* (Figure 5C). Using control human myoblast cell lines and muscle biopsies, we showed that *LMOD3* was expressed soon after the start of myoblast differentiation and in skeletal muscle throughout life from at least 14 weeks gestation (Figure 5, A and B).

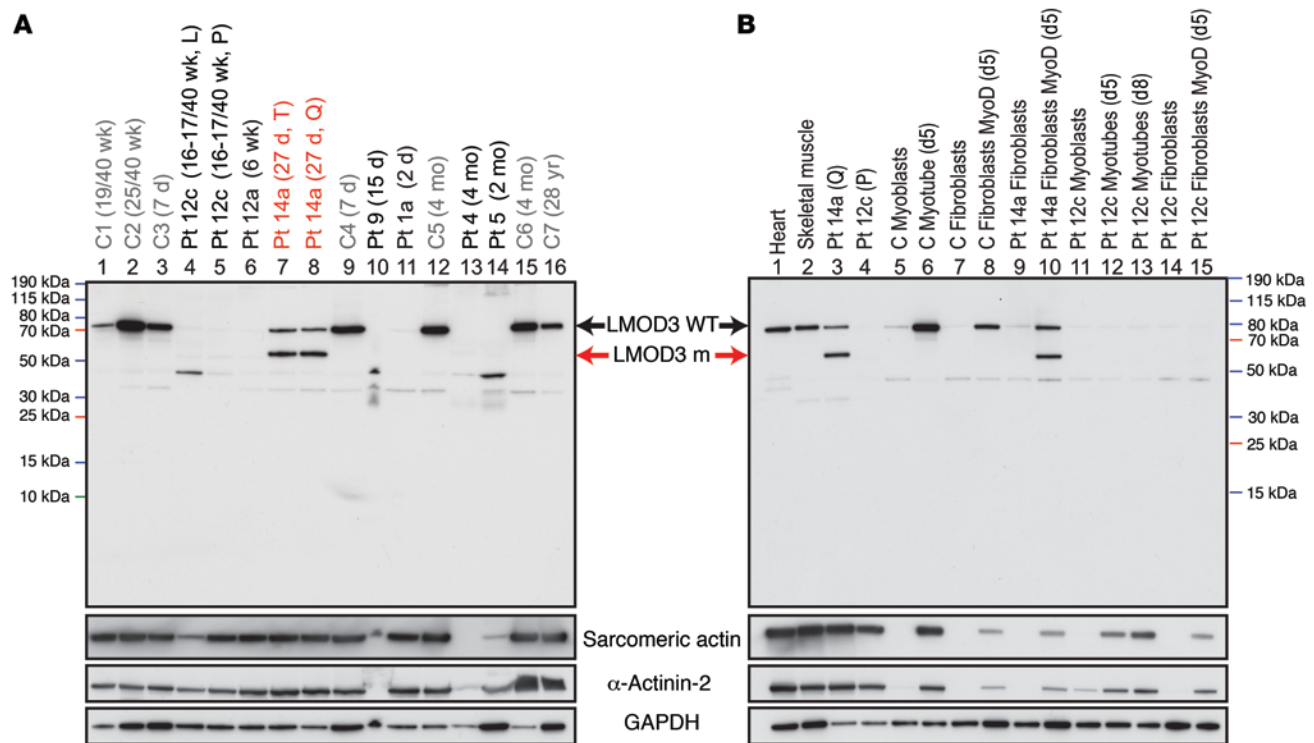


**Figure 2. Most *LMOD3* mutations abolish *LMOD3* protein expression.** Western blots assessing *LMOD3* expression in available (A) patient muscle tissue and (B) patient primary muscle cells. (A) In most patients with nonsense or frame-shift mutations, truncated protein of the predicted size were not detected. In some biopsies, replacement of muscle tissue by connective tissue may limit our ability to detect a muscle-specific truncated product (e.g., lanes 4, 10, 13, and 14; expression of sarcomeric actin and  $\alpha$ -actinin-2 is low relative to that of GAPDH). Muscle from patient 14a shows expression of truncated protein from both mutant *LMOD3* alleles (red arrow, mutations in red in Figure 1). The approximately 50-kDa band (lanes 4, 10, and 14 and weakly in controls) does not correlate with the predicted molecular weight of mutant *LMOD3* in these patients (12–43 kDa). This band likely arises from Ab cross-reactivity with a nonmuscle *LMOD* isoform or an unrelated nonmuscle antigen. (B) Primary myoblasts were differentiated into myotubes, and primary fibroblasts were MyoD-converted into differentiated myotubes in culture. Primary cells from controls express *LMOD3* (~80-kDa band) and other thin filament markers (sarcomeric actin and  $\alpha$ -actinin-2) after 5 days (d5) of differentiation (lanes 6 and 8). Myogenic conversion of fibroblasts from patient 14a induces expression of mutant *LMOD3* from both alleles (lane 10; R401\*, red arrow). Primary myotubes and MyoD-converted fibroblasts from patient 12c (homozygous p.N367Qfs\*11) express no mutant protein (lanes 12, 13, and 15). These results replicate *LMOD3* expression obtained in patient and control muscle biopsies. L, leg muscle; P, paraspinalis muscle; Q, quadriceps; T, triceps.

Localization of *LMOD3* within skeletal muscle sarcomeres was assessed by immunolabeling of stretched adult human control muscle and differentiated cultured control myotubes. *LMOD3* was highly expressed in nonstriated areas of developing myotubes and showed a granular cytoplasmic staining (Figure 5, D and E, square 2). In areas in which myosin and actin filaments were organized into sarcomeres, *LMOD3* showed intense staining of the M band region, which colocalizes with thin filament pointed ends in unstretched sarcomeres. Less intense staining was observed along thin filaments, and the Z-discs were unstained (Figure 5, D and E, square 1). Expression of mCherry-labeled *LMOD3* in cultured quail myotubes provides additional evidence for localization to the M line/thin filament pointed end region (Supplemental Figure 4).

In stretched mature human skeletal muscle, we observed 3 staining patterns: (a) exclusive staining near the pointed end of thin filaments, (b) combined staining near the pointed end and along the thin filament, and (c) predominant staining along the thin filament (Supplemental Figure 5). In 4 of 5 biopsies, we observed more than one staining pattern in different myofibers, and no correlation with fiber type (determined by myosin heavy

chain [MHC] analysis) or age was found (Supplemental Figure 6). We compared the breadth of *LMOD3* staining across a full sarcomere to the thin filament length, measured using phalloidin in the same sarcomere, and found that, while they closely correlated in fast fibers, the breadth was significantly shorter in slow fibers ( $P < 0.0001$ , paired  $t$  test). This suggests that *LMOD3* binding may extend to the thin filament cap in fast fibers but ends before the cap in slow fibers (Figure 6, E and F). When the *LMOD3* signal was enriched near the pointed end, the band appeared wider than those obtained for *TMOD1* and *TMOD4*. At higher magnification, the wide *LMOD3* band could occasionally be resolved into 2 narrow bands (Figure 6D and refs. 8, 9). The intense *LMOD3* stained peak near the pointed end was further away from the Z-disc in fast myofibers ( $1.07 \pm 0.13 \mu\text{m}$ ,  $n = 14$ ) compared with slow myofibers ( $0.91 \pm 0.14 \mu\text{m}$ ,  $n = 15$ ,  $P = 0.0044$ ,  $t$  test; Figure 6E). Notably, the peak of *LMOD3* staining in both myofiber types was significantly closer to the Z-disc than that of *TMOD1* (average of fast and slow myofibers), which was located  $1.26 \pm 0.16 \mu\text{m}$  ( $n = 4$ ) from the Z-disc, suggesting that *LMOD3* may be located near, but not at, the thin filament pointed end.

**Table 2. Clinical features of LMOD3-NM**

Patient ID	Genotype	Ethnicity	Sex	Clinical subtype <sup>a</sup>	Clinical features
1a	p.S47fs*13	Algerian	F	SC	Deceased (neonatal period) <sup>b</sup> . Polyhydramnios, preterm delivery (30/40), arthrogryposis, fractures (bilateral femoral).
1b	p.S47fs*13	Algerian	F	SC	Deceased (neonatal period). Preterm delivery (36/40).
2	p.S47fs*13	Belgian	M	SC	Deceased (10 months). Decreased fetal movements, breech presentation, arthrogryposis, ophthalmoplegia.
3a	p.M52*	Portuguese	F	SC	Deceased (neonatal period). Polyhydramnios, decreased fetal movements, contractures.
3b	p.M52*	Portuguese	F	SC	Alive at 1 month, lost to follow-up. Polyhydramnios, contractures.
4	p.W77*	Japanese	M	SC	Alive at 4 months, lost to follow-up.
5	p.T101Rfs*4 / p.D201Efs*9	Japanese	F	SC	Alive at 2 months, lost to follow-up. Polyhydramnios, decreased fetal movements, subdural hematoma.
6	p.Q117*	Japanese	F	SC	Alive at 10 months, lost to follow-up. Polyhydramnios, decreased fetal movements, fetal edema, preterm delivery (32/40), microcephaly, contractures.
7	p.Q117* / p.K406Nfs*11	Japanese	F	SC	Alive at 1 year 7 months, lost to follow-up. Polyhydramnios, decreased fetal movements, ophthalmoplegia.
8	p.D242Efs*4 / p.G326R	South American	F	SC	Deceased (neonatal period).
9	p.F287Sfs*3	Italian	F	SC	Deceased (4 months). Polyhydramnios, decreased fetal movements, preterm delivery (34/40), ophthalmoplegia, contractures.
10	p.G326R / p.Q458*	Ecuadorian	M	SC	Deceased (6 weeks). Polyhydramnios, decreased fetal movements, preterm delivery (35/40), breech presentation, ophthalmoplegia, arthrogryposis, fractures (bilateral humeral).
11a	p.E357*	Swedish	M	SC	Deceased (5 months). Polyhydramnios, arthrogryposis.
11b	p.E357*	Swedish	M	SC	Deceased (neonatal period).
12a <sup>c</sup>	p.N367Qfs*11	Afghani	M	SC	Deceased (2 months). Absent fetal movements, preterm delivery (31/40), breech presentation, arthrogryposis.
12b	p.N367Qfs*11	Afghani	M	SC	Deceased (neonatal period). Preterm delivery (33/40), arthrogryposis.
12c	p.N367Qfs*11	Afghani			Affected fetus.
13a	p.N367Qfs*11	Pakistani	F	SC	Deceased (3 months). Polyhydramnios, breech presentation, ophthalmoplegia, kyphosis.
13b	p.N367Qfs*11	Pakistani	F	SC	Deceased (neonatal period). Polyhydramnios, decreased fetal movements.
14a	p.N367del / p.R401*	Australian	F	TC	Alive (10 years). Polyhydramnios, decreased fetal movements, bulbar weakness, ophthalmoplegia, percutaneous endoscopic gastrostomy, nocturnal noninvasive ventilation. Walks independently. Normal cardiac assessment and echocardiogram.
14b	p.N367del / p.R401*	Australian	F	TC	Alive (4 years). Polyhydramnios, bulbar weakness, percutaneous endoscopic gastrostomy, nocturnal noninvasive ventilation. Walks with truncal support. Normal cardiac assessment and echocardiogram.

<sup>a</sup>Classification of clinical subtype of NM relates to the European Neuromuscular Centre classification of NM (1). <sup>b</sup>Neonatal period indicates less than 28 days of age. <sup>c</sup>Corresponds to BOS-1120. TC, typical congenital NM; SC, severe congenital NM; F, female; M, male; 30/40, gestational age of 30 weeks.

*LMOD3 is a potent actin nucleator and has a weaker binding affinity to tropomyosin compared with that of LMOD2.* Previous studies have shown that LMOD2 localizes to the pointed end of actin filaments in cardiomyocytes and is a potent actin filament nucleator (10–12). We used a pyrene actin nucleation assay to compare the actin nucleation properties of LMOD2 and LMOD3 and observed that both leiomodins led to a marked increase in rate of actin polymerization, with an equivalent dose dependence (Figure 7A).

The leiomodins share a single tropomyosin (TM) binding domain with TMOD, and amino acid sequence analysis showed that LMOD3 is more divergent from TMOD1 than LMOD2 in this region (Figure 1 and Supplemental Figure 7, amino acids 29–40 in LMOD3). We performed far-UV circular dichroism (CD) spectral studies to test binding of an N-terminal  $\alpha$ -TM peptide to LMOD2 and LMOD3 peptides. CD spectral studies indicated complex formation for TM/LMOD2 and TM/LMOD3 peptide mixtures (Figure 7C). The increase in  $\alpha$ -helicity was stronger for LMOD2,

indicating a higher TM binding affinity. Unfolding curves of TM/LMOD peptide complexes indicated that the LMOD2 peptide binds approximately 4-fold more strongly to the  $\alpha$ -TM N-terminal peptide than the LMOD3 peptide ( $K_D = 3.5 \pm 0.5 \mu\text{M}$  for TM/LMOD3 and  $0.9 \pm 0.3 \mu\text{M}$  for TM/LMOD2,  $n = 3$ ; Figure 7B).

*Thin filament structure is altered in patients with LMOD3-NM and lmod3 KO zebrafish.* We assessed thin filament architecture in LMOD3-NM by dissecting longitudinal myofiber bundles from 9 patient biopsies and staining stretched bundles with phalloidin, which labels filamentous actin (Figure 8, A–J). In half of the biopsies we found no discernible sarcomeric structure (patients 4, 5, 6, and 9). In all other patient biopsies we observed varying degrees of thin filament shortening and disorganization (patients 1a, 7, 12a, 14a; Supplemental Table 2). Four biopsies from three patients (patients 1a, 12a, and 14a) also contained regions with well-organized sarcomeres, and such regions were also seen on EM images (Figure 3, G and H).

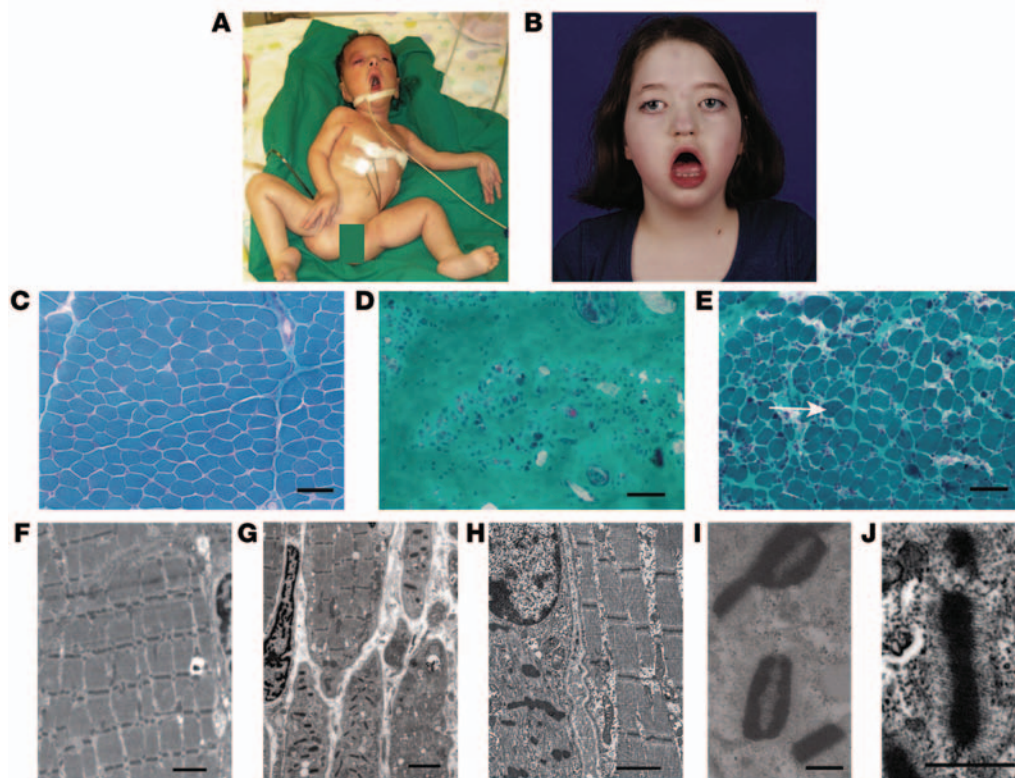


**Figure 3. Clinical and histological features in NM due to *LMOD3* mutations.** (A and B) Photographs of patients with *LMOD3*-NM. (A) Most affected individuals had severe generalized muscle weakness and hypotonia at birth and died in infancy (patient 9, severe congenital NM). (B) Patient 14a has less severe weakness and has survived into childhood. Note the severe facial and jaw weakness. (C) Control Gomori trichrome image (5-month-old child). (D and E) Skeletal muscle biopsy findings in (D) patient 6 and (E) patient 4. (D) Some biopsies had only a few scattered atrophic myofibers within abundant connective tissue. Nemaline bodies appear as purple or blue inclusions (arrow). (F) Control EM image (6-week-old child, rectus abdominis muscle). (G and H) EM images from some patient biopsies show myofibers with ordered sarcomeres adjacent to myofibers with disordered sarcomeres and thickened Z-discs. (I and J) Many nemaline bodies appear as thickened Z-discs, (I) sometimes in pairs interconnected by thin filaments. Some nemaline bodies resemble thickened Z-discs surrounded by a short thin filament “fringe.” Images show (G and J) patient 12a, (H) patient 14a, and (I) patient 1a. Scale bar: 50  $\mu$ m (C–E); 2  $\mu$ m (F–H); 500 nm (I and J).

Ultrastructural analysis of skeletal muscles from *lmod3* MO zebrafish also showed regions with ordered sarcomeres when *LMOD3* was knocked down. Electron micrographs of zebrafish skeletal muscle showed subtle differences in appearance around the M line in *lmod3* MO zebrafish compared with controls (Supplemental Figure 3, A and B). This could represent either loss of the border of the H zone, which relies on well-aligned thin filament pointed ends (see Supplemental Figure 3C) or, alternatively, could be due to abnormal organization of myosin thick filaments.

To further investigate whether dysregulation of thin filament length contributes to muscle weakness in *LMOD3*-NM, we isolated myofiber bundles from *LMOD3*-NM patient and control muscle biopsies and measured the force to sarcomere length (SL) relationship. In normal muscle, actin filament length is tightly controlled to ensure optimal thin-thick filament overlap for efficient force generation at optimal muscle stretch. At SLs greater than approximately 2.6  $\mu$ m, the overlap of the contractile filaments decreases, resulting in a linear decrease of force production (descending limb). Assuming a constant thick filament length, the shape of the force/SL curve is determined by the length of the thin filament (13).

We were able to perform force measurements at SLs of 2.0 to 3.5  $\mu$ m in the 3 biopsies from patients 14a and 12a, the biopsies with the best sarcomeric organization (Figure 8, K–M). Highly variable contractile force (patient 1a) or no measurable force (patients 4 and 7) was obtained in other biopsies, likely because muscle structure was too disordered. Interestingly, maximal force normalized to cross-sectional area in both biopsies from patient 14a was the same as that in controls (mean force:  $62.06 \pm 15.82$  and  $61.25 \pm 19.56$  mN/mm<sup>2</sup> in patient myofibers and  $61.94 \pm 22.07$  mN/mm<sup>2</sup> in 5 controls), while patient 12a myofibers produced 57% less force than controls ( $26.72 \pm 6.34$  mN/mm<sup>2</sup>;  $P < 0.0001$ ) (Figure 8K). In all 3 biopsies, there was a leftward shift in the force/SL curve, consistent with decreased thin filament lengths in these patients (Figure 8L). Patient 12a produced less specific force at all SLs.

*Several thin filament pointed end proteins are dysregulated in *LMOD3*-NM.* We investigated the expression of *LMOD2*, another striated muscle leiomodin, and the 2 sarcomeric

skeletal muscle tropomodulins, *TMOD1* and *TMOD4*, in available patient muscle biopsies using Western blot analysis. We found increased *LMOD2* expression in all patients tested, compared with age-matched control biopsies. *TMOD1* expression was variable in both groups, and *TMOD4* expression was uniformly decreased in patient biopsies (Figure 9). *TMOD1* and *TMOD4* immunostaining on stretched patient bundles showed that both proteins still localized to the pointed end of thin filaments in myofibrils with discernible sarcomeric structure (Supplemental Figures 8 and 9). However, in the fiber bundles extracted from muscle from patient 12a, *TMOD1* labeling was enriched in some areas containing protein accumulations (Supplemental Figure 8). *LMOD2* and *LMOD3* staining was not consistently detected in stretched bundles from either controls or patients, suggesting that the process of preparing stretched myofiber bundles from frozen biopsies disrupts staining with these Abs, unfortunately.

## Discussion

We describe 21 patients from 14 families who have compound heterozygous or homozygous mutations in *LMOD3* consistent with

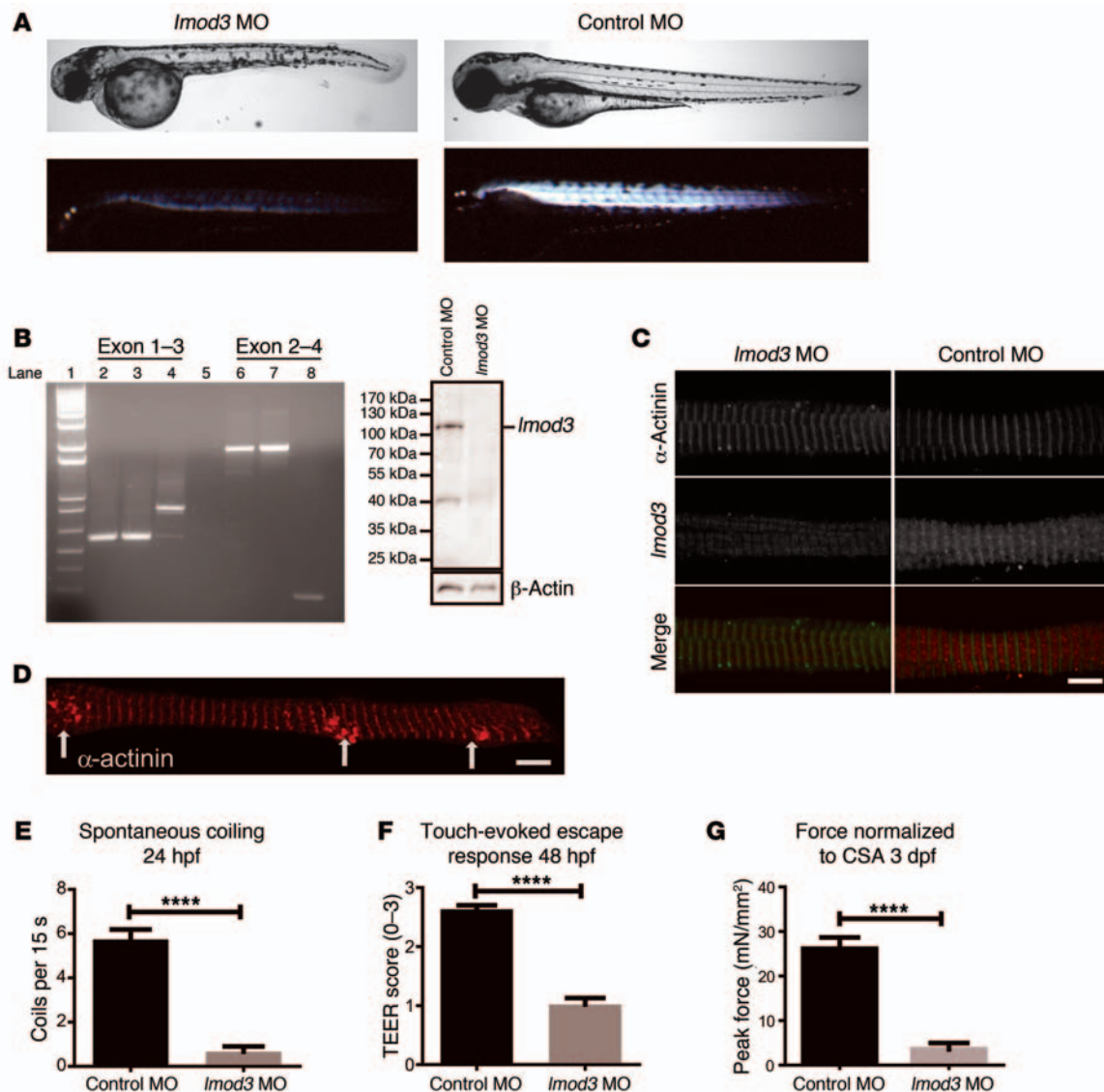


**Figure 4. Morpholino knockdown of *Imod3* in zebrafish recapitulates features of *LMOD3*-NM.** (A) Representative bright-field (top) and birefringence (bottom) images of control and *Imod3* knockdown zebrafish morphants 3 days after fertilization (dpf). Note the shorter body size, bent tail, and reduced birefringence of *Imod3* MO. (B) RT-PCR from embryos injected with control morpholinos (lanes 2, 3, 6, and 7) or *Imod3* morpholinos (lanes 4 and 8). Knockdown of the *Imod3* gene was achieved using 2 morpholinos directed against different splice sites. PCR, performed with primers targeting *Imod3* spanning exons 1-3 (lanes 2-4) and exons 2-4 (lanes 6-8), demonstrates successful interruption of splicing by the *Imod3* morpholinos. *LMOD3* protein expression was markedly reduced in *Imod3* MO embryos by (B) Western blotting and (C) immunohistochemistry. (D) Isolated myofibers from *Imod3* MO immunostained with  $\alpha$ -actinin show protein accumulations resembling nemaline bodies (white arrows). No accumulations were observed in control MO (data not shown). (E) Spontaneous embryo coiling 24 hours after fertilization (hpf) was significantly reduced in *Imod3* MO. (F) A significant reduction in touch-evoked escape response (0-3 response scale) was observed 48 hours after fertilization in *Imod3* MO. (G) Contractile force generated by *Imod3* MO trunk muscle (3 days after fertilization) was significantly reduced. All error bars represent mean  $\pm$  SEM. Scale bar: 5  $\mu$ m (C and D). \*\*\*\* $P$  < 0.0001, 2-tailed paired  $t$  test. CSA, cross-sectional area.

autosomal recessive inheritance, associated with severe NM, establishing *LMOD3* as a new cause of this disorder. As further confirmation, we developed a zebrafish model of *LMOD3*-NM and demonstrated abnormalities in skeletal muscle organization and function after *LMOD3* knockdown.

The clinical presentation of *LMOD3*-NM is characterized by early-onset severe generalized muscle weakness and hypotonia, with respiratory insufficiency and feeding difficulties. The severe congenital subtype of NM is relatively uncommon, accounting for only 16% of patients with NM in a large case series (14). Ninety per-

cent of patients with *LMOD3*-NM identified in the current study had severe congenital NM, establishing *LMOD3* as an important cause of this phenotype, in addition to *ACTA1*, *NEB*, *KLHL40*, and *KLHL41*. Features commonly seen in *LMOD3*-NM, which may serve as clinical clues for the disorder, include arthrogryposis or congenital contractures, ophthalmoplegia, and a history of prematurity, reduced fetal movements, and polyhydramnios. We also report a distinctive ultrastructural appearance of nemaline bodies in *LMOD3*-NM. Many of the nemaline bodies resembled thickened Z-disc remnants, which often appeared in pairs, surrounded

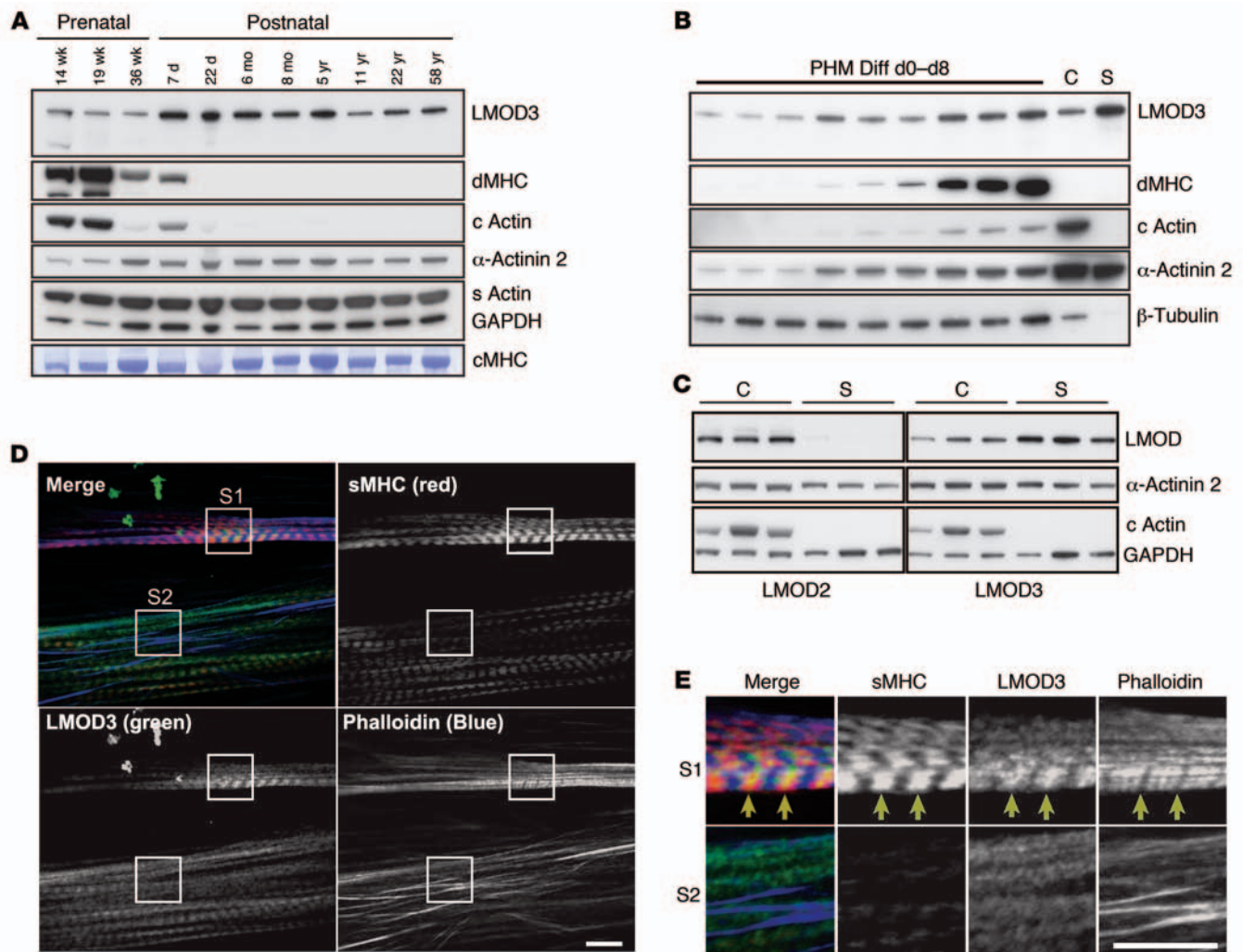


**Figure 5. LMOD3 expression in human muscle tissue and primary cells.** LMOD3 expression during muscle cell differentiation and muscle development in (A) human skeletal muscle tissue and (B) differentiating primary human myoblasts. (A) In skeletal muscle, LMOD3 was detected at all ages tested (assessed age range: 14 weeks gestation to 58 years), but expression before birth was lower than that in mature muscle. Developmental MHC (dMHC) and cardiac actin (c actin) were expressed in fetal muscle biopsies as expected. Sarcomeric actin (s actin),  $\alpha$ -actinin-2, GAPDH, and MHC (Coomassie-stained MHC [cMHC]) served as loading controls. (B) LMOD3 was detected weakly in undifferentiated human myoblasts (day 0 [d0]), and levels increased during differentiation into myotubes similar to other muscle proteins, such as  $\alpha$ -actinin-2, developmental MHC, and cardiac actin.  $\beta$ -Tubulin served as a loading control. PHM Diff, primary human myoblasts differentiation. (C) LMOD2 and LMOD3 expression in mature human cardiac muscle and skeletal muscle. LMOD3 expression was higher in skeletal muscle than in heart, while the reverse was true for LMOD2. (D) Localization of LMOD3 in primary human myoblasts at day 10 of differentiation by confocal imaging. (E) Magnified view of white squares in D. Square 1 (S1) shows a striated area, demonstrating that LMOD3 was most abundant at the thin filament pointed end and/or M line, which colocalize in unstretched sarcomeres, and was absent from the Z-disc (yellow arrows). In square 2 (S2), LMOD3 staining appears granular in areas where striations have not formed. Scale bar: 7.5  $\mu$ m (D and E). C, human heart; S, postnatal human skeletal muscle.

by highly shortened thin filaments. This appearance is rare in other forms of NM and may assist in diagnosing this condition. Interestingly, even though we demonstrated that LMOD3 is present in cardiac muscle, cardiac involvement has not been reported so far in *LMOD3*-NM, and it is possible that LMOD2 may compensate for loss of LMOD3 in cardiac muscle.

Most *LMOD3* mutations we identified are nonsense or frameshift mutations that would truncate the LMOD3 protein if expressed. In almost all patients with *LMOD3*-NM for whom muscle biopsies were available, mutations in *LMOD3* were associated with a loss of LMOD3 expression. The only exception was family 14, in which we found expression of both the p.N367del

and p.R401\* mutant LMOD3 alleles in skeletal muscle. Patients 14a and 14b are the only 2 patients known to have survived beyond early childhood, which suggests that one of these mutant proteins (or both) retains some function, conferring a milder phenotype. The fact that loss of LMOD3 leads to severe muscle dysfunction indicates that LMOD3 plays an essential role in skeletal muscle, which has not been recognized previously.

A striking feature in muscles from many patients with *LMOD3*-NM is replacement of myofibers with connective tissue. After staining of actin filaments in individual myofibers with phalloidin, no discernible sarcomeres were seen in half of the patient muscle biopsies, indicating widespread disorganization of muscle ultra-

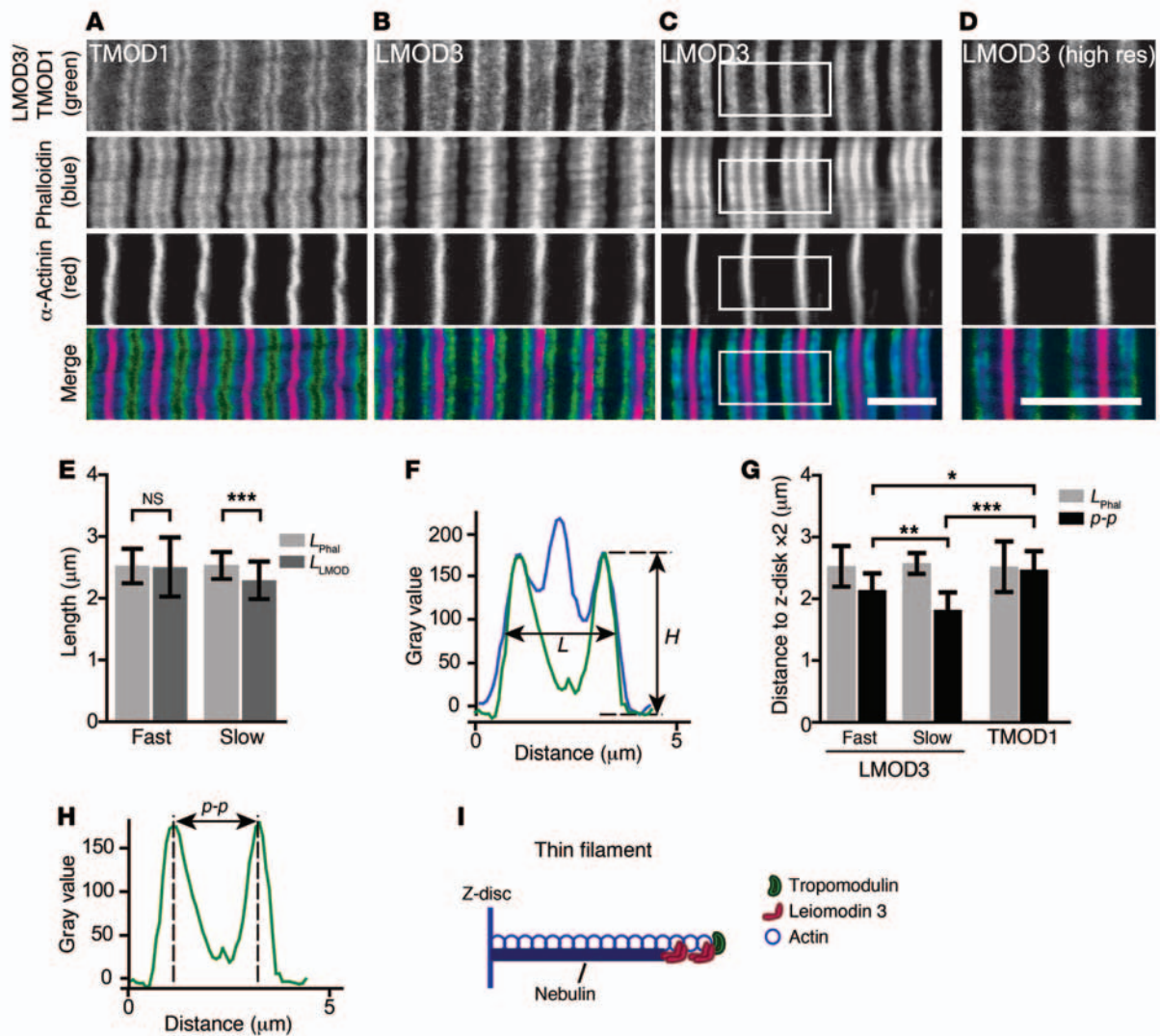


**Figure 6. LMOD3 localizes to actin thin filaments in the muscle sarcomere.** (A) TMOD1 pointed end localization and (B and C) 2 examples of LMOD3 localization in stretched human control quadriceps muscles. Actin filaments were colabeled with Alexa Fluor 488-conjugated phalloidin (blue),  $\alpha$ -actinin (Z-discs, red), and LMOD3 (green). (D) At higher magnification, LMOD3 pointed end staining can occasionally be resolved into 2 distinct bands. (E) Measurements of LMOD3 and phalloidin signal breadth taken at the half peak height ( $L_{\text{LMOD}}$  and  $L_{\text{Phal}}$ , respectively), using methods illustrated in F.  $L_{\text{LMOD}}$  and  $L_{\text{Phal}}$  are indistinguishable in fast fibers (NS, paired  $t$  test), but  $L_{\text{LMOD}}$  is shorter than  $L_{\text{Phal}}$  in slow fibers (\*\*\*)  $P < 0.0001$ , paired  $t$  test), suggesting that LMOD3 binding ends before the pointed end cap in slow fibers. (G) Measurements of the distance between the LMOD3 peak located near the pointed end and the Z-disc (fast and slow fibres) and the distance between the TMOD1 peak and the Z-disc ( $p-p$ , peak-to-peak), as illustrated in H. Thin filament lengths were measured in the same sarcomeres from phalloidin staining, as illustrated in F. The peak of the LMOD3 signal was significantly closer to the Z-disc in slow myofibers (\*\*\*)  $P = 0.0009$ , 2-tailed unpaired  $t$  test) and fast myofibers ( $*P = 0.0472$ , 2-tailed unpaired  $t$  test) as compared with TMOD1. The peak of LMOD3 staining localized closer to the Z-disc in slow muscle myofibers compared with fast myofibers (\*\*  $P = 0.0043$ , 2-tailed unpaired  $t$  test). (I) Diagram showing the hypothesized positions of LMOD3 pointed end binding relative to other thin filament proteins. Scale bar: 7.5  $\mu\text{m}$ . Graphs show mean  $\pm$  SD.

structure. A paucity of contractile units is likely the main cause of muscle weakness in most patients. When sarcomeres were present, a range of structural abnormalities were seen, ranging from thickened Z-disc-like structures without thin filaments, to Z-discs with shortened thin filaments, to sarcomeres with near-normal structure. In addition, *mod3* MO zebrafish lacked clearly defined pale zones immediately adjacent to M lines. This appearance could be caused by abnormal myosin filament/M line structure or due to loss of distinct H bands, a finding reported in *Neb* knockout mice (15). The H zone represents the region of the sarcomere that only contains thick filaments, with the H zone boundary created by the well-aligned thin filament pointed ends at either side. In

*Neb* knockout mice, variability in thin filament lengths leads to loss of a clear boundary for the H zone (15). To obtain further information about whether variable thin filament lengths may be a common finding in *LMOD3*-NM, we analyzed the force/SL relationship in myofibers dissected from patient biopsies. The leftward shift in the force/SL curves in all biopsies tested confirms that, even in myofibers with well-ordered sarcomeres, populations of shortened thin filaments are present and likely contribute to muscle weakness, a mechanism of disease previously linked to other forms of NM (16). Dysregulation of the tropomodulins, particularly TMOD4, in skeletal muscle, may also contribute to muscle weakness in *LMOD3*-NM.

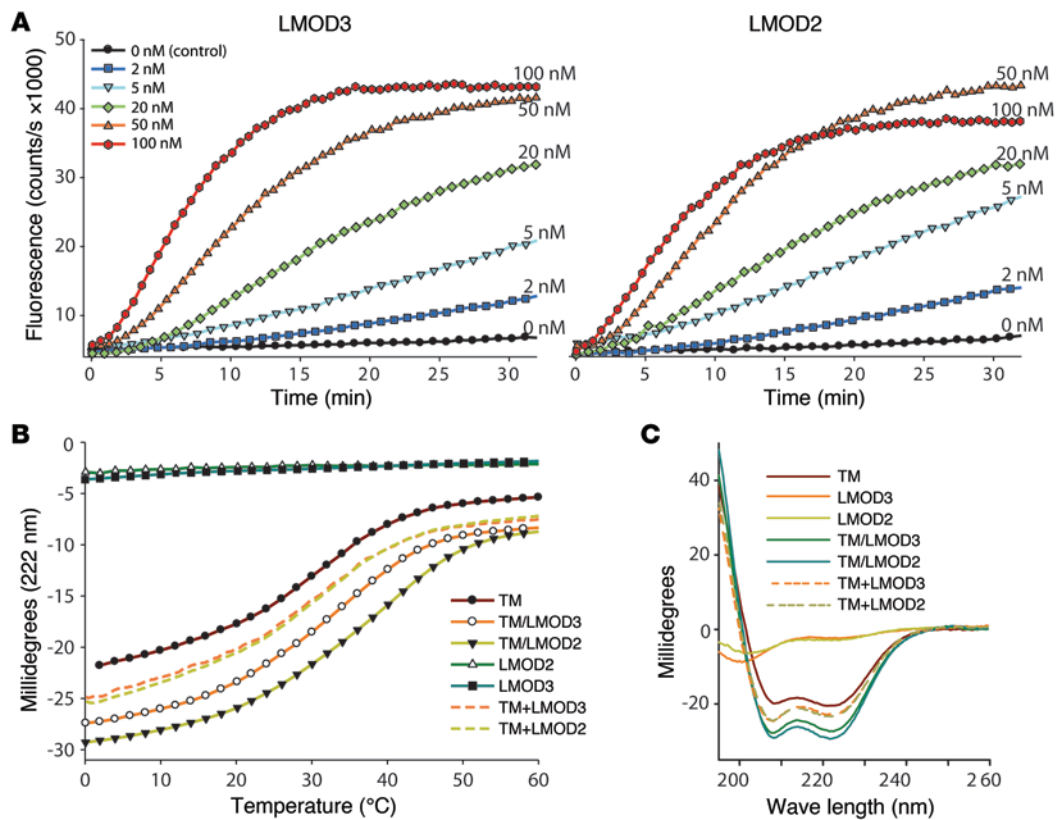


**Figure 7. Actin nucleation activity and TM binding of LMOD2 and LMOD3.** (A) Nucleation/polymerization time course of 1.1  $\mu\text{M}$  G-actin (10% pyrenyl-actin) after addition of polymerization buffer containing different concentrations of LMOD2 or LMOD3. LMOD2 and LMOD3 increase actin polymerization/nucleation to a similar extent, compared with spontaneous actin nucleation/polymerization. (B) Binding of LMOD2 and LMOD3 peptides to TM peptides measured using CD spectroscopy. The graph shows the unfolding curves for individual peptides (e.g., TM, LMOD2, LMOD3), their mixture (TM/LMOD2, TM/LMOD3), and the sum of individual unfolding curves (TM+LMOD2, TM+LMOD3). The dissociation constants ( $K_d$ ) of the peptide complexes were  $3.5 \pm 0.5 \mu\text{M}$  ( $n = 3$ ) for TM/LMOD3 and  $0.9 \pm 0.3 \mu\text{M}$  ( $n = 3$ ) for TM/LMOD2 (binding of LMOD3 to skeletal muscle TM is  $\sim 4$  times weaker than that of LMOD2,  $P = 0.0018$ , 2-tailed  $t$  test). (C) Far-UV CD spectra for synthetic peptides corresponding to the TM-binding sites of LMOD3 and LMOD2 and the model TM peptide, TM1aZip, their mixtures, and the sums of the individual spectra (10  $\mu\text{M}$  each, measured in 1-mm cuvettes at  $10^{\circ}\text{C}$  in 10 mM Na-Phosphate buffer, pH 7.0, 100 mM NaCl). Based on shapes of the spectra for LMOD2 and LMOD3 peptides,  $\alpha$ -helix/random coil ratio is lower for LMOD3 peptide, suggesting it is less structured. The difference between the spectra of the TM/LMOD mixtures and the sums of corresponding individual spectra (TM+LMOD) demonstrates the increase in helicity and therefore indicates complex formation. The effect is stronger for LMOD2.

The N-termini of LMOD1, LMOD2, and LMOD3 have approximately 40% sequence identity with the TMODs, sharing 2 actin-binding domains and 1 of 2 TM-binding sites (10). In addition, the C-termini of the leiomodins contain a third actin-binding domain, which is not present in the TMODs but which is a characteristic of actin filament-nucleating proteins (Figure 1 and ref. 10). Previous studies have shown that LMOD2 localizes near the pointed end of thin filaments in cardiomyocytes and functions as a potent actin filament nucleator in vitro (10–12).

To investigate the biological functions of LMOD3, we performed a range of studies in control muscle samples and using recombinant protein. Tsukada et al. showed that LMOD2 regulates thin filament lengths in cardiomyocytes likely by competing with TMOD, which caps actin filaments, and by promoting actin polymer extension at the pointed end of thin filaments (12). We hypothesized that LMOD3 may play a similar role in skeletal muscle. Our studies using recombinant proteins and stretched quadriceps muscle show that, like all other members of the TMOD family, LMOD3 binds both actin and TM and localizes close to the

pointed ends of thin filaments, a key site for actin turnover and control of thin filament length in skeletal muscle. We also demonstrated that LMOD3, like LMOD2, is an effective catalyst of actin nucleation. In addition, loss or dysfunction of LMOD3, which defines *LMOD3-NM*, was associated with short thin filaments in immunofluorescent and force/SL measurement studies in patient myofibers. These data are all consistent with a central role for LMOD3 in modulating thin filament length in skeletal muscle.

In *LMOD3-NM* patient muscle, we observed an upregulation of LMOD2, another striated muscle leiomodins that is expressed at higher levels in cardiac muscle compared with skeletal muscle. This may represent a specific upregulation of a homologous protein as a compensatory mechanism, a process that is well described to occur in patients with autosomal recessive mutations in *ACTA1*, which encodes  $\alpha$ -skeletal actin, in whom cardiac actin is markedly upregulated in skeletal muscles after birth (17, 18). However, the presence of such severe muscle weakness in patients with *LMOD3-NM* suggests that the LMOD2 upregulation that occurs compensates poorly for the loss of functional LMOD3. The fact

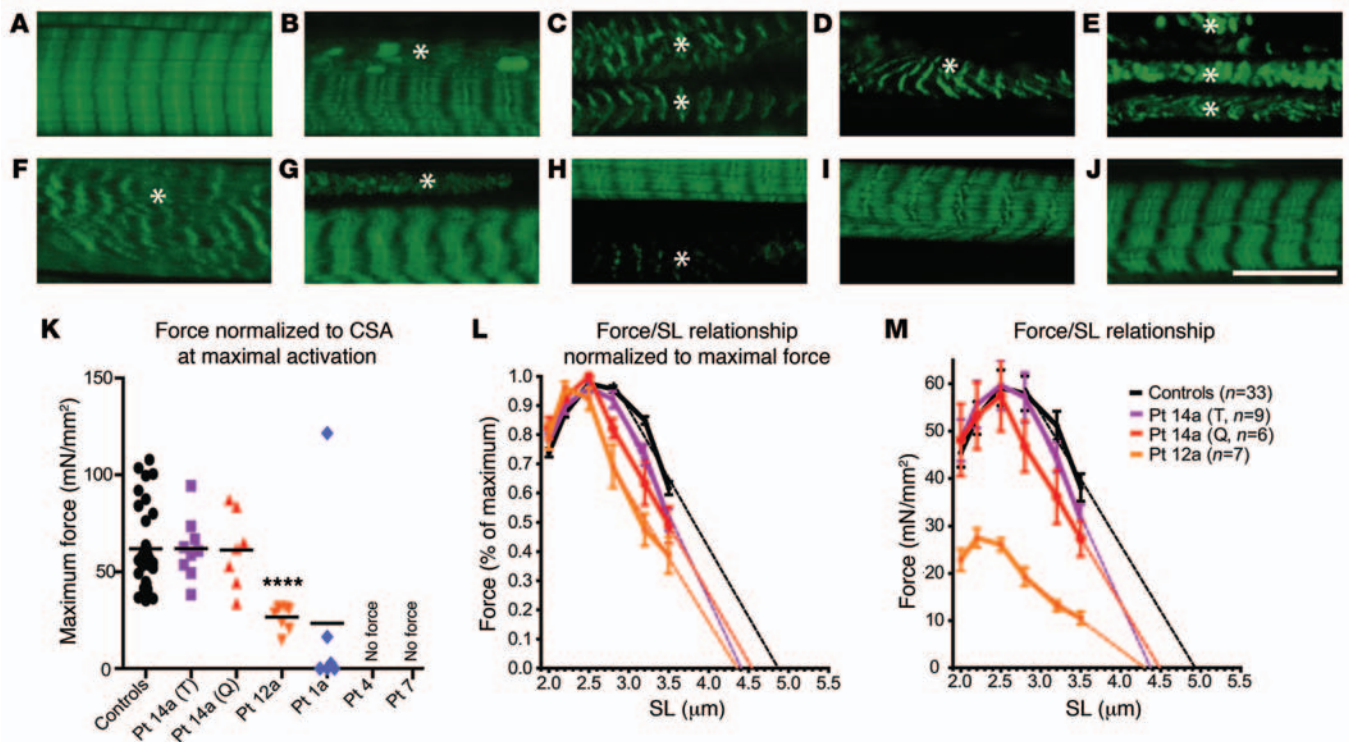


**Figure 8. Patient myofibers show evidence of shortened/disorganized thin filaments.** (A–J) Phalloidin-stained stretched myofiber bundles dissected from human *LMOD3*-NM patient biopsies. Thin filaments are well aligned and have consistent lengths in (A) controls and (I and J) some areas of patient muscle. (B–H) Representative images of patient muscles demonstrate moderate/severe sarcomere disorganization (asterisks), (C, D, and H) Z-discs with short protruding thin filaments, and (E and F) thickened Z-discs. Images show (A) control, (B and J) patient 14aQ, (C) patient 1a, (D and E) patient 7, (F and G) patient 14aT, and (H and I) patient 12a. (K) Maximal specific force (force/cross-sectional area) measurements at optimal SL (patient 12a: 2.2 μm; patient 14a and controls: 2.5 μm) in permeabilized myofiber bundles was normal in patient 14a compared with controls ( $n = 5$ ), while patient 12a generated significantly less force (\*\*\*\* $P < 0.0001$ , 2-tailed  $t$  test). Force/SL curves (L) normalized to maximal force or (M) absolute force showed a leftward shift consistent with reduced force at longer SL in patients (patient 12a SL > 2.8,  $P < 0.001$ ; patient 14aQ SL = 2.8, 3.2, and 3.5,  $P < 0.01$ ,  $P < 0.001$ , and  $P < 0.05$ , respectively; patient 14aT SL > 3.2,  $P < 0.05$ ; 2-way ANOVA). Error bars represent SEM. Scale bar: 10 μm.

that LMOD2 and LMOD3 have different TM-binding affinities and the fact that LMOD2 does not compensate for the loss of LMOD3 in *LMOD3*-NM suggest that, even though many properties are similar, there may be important differences in biological function between these proteins.

In stretched mature control muscle, LMOD3 staining was enriched in a wide band close to the pointed end of thin filaments. The distance of the staining peak from the Z-disc was different in slow and fast myofibers, raising the possibility that LMOD3 has different roles in the 2 myofiber types. LMOD3 staining differed from TMOD1 staining in several ways. LMOD3 staining near the pointed end was broader than for TMOD1 and the peak was closer to the Z-disc. These differences suggest that LMOD3 may not simply act as a competitive binding partner with TMOD1 for the pointed end, as has been proposed for LMOD2 (12). In addition, in approximately 50% of myofibers, staining was not restricted to the pointed end but was also present along thin filaments. Fiber type and biopsy age were not responsible for this variability, and the factors that determine the position of LMOD3 binding in different myofibers have yet to be identified. Studies of LMOD2 have also found evidence of a variable localization, and, in the case of LMOD2, localization appeared responsive to muscle contraction (11). The evidence we present for variable localization suggests that LMOD3

may have several functions; it may bind near the pointed end of thin filaments to modulate filament length and also bind along the length of the thin filament to perhaps function as a thin filament stabilizer. Further studies are required to confirm this hypothesis.

In a recently published study, LMOD3 and nebulin were identified as major binding partners of KLHL40, loss of which results in a severe lethal form of NM associated with destabilization of thin filament proteins (19, 20). KLHL40 was found to promote stability of LMOD3 by blocking its ubiquitination, and loss of KLHL40 was associated with almost complete absence of LMOD3 protein in skeletal muscles of mice and KLHL40-deficient patients. These data support a pivotal role for LMOD3 in the stability of the sarcomere thin filament. The newly identified interaction among LMOD3, nebulin, and KLHL40 provides the “missing link” between thin filament proteins and the kelch (BBK) protein family and suggests a common pathway for the pathogenesis of a number of different genetic forms of NM.

In conclusion, we show that autosomal recessive mutations in *LMOD3* are a new and important cause of severe congenital NM and that LMOD3 plays a critical role in skeletal muscle biology. Multiple lines of evidence point to a role for LMOD3 as a key regulator of thin filament length in skeletal muscle. This study emphasizes the power of WES in identifying the genetic basis of

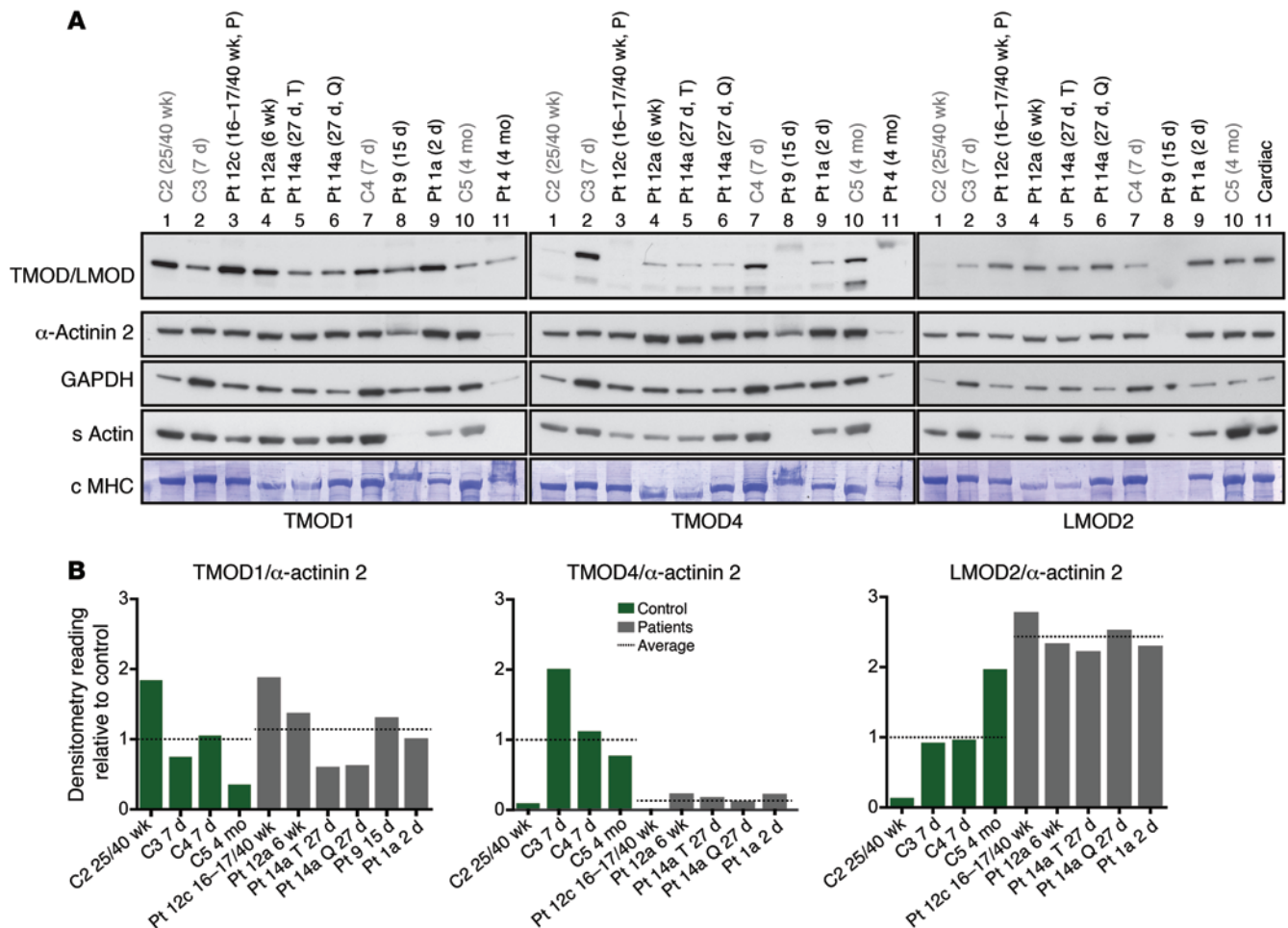


**Figure 9. Levels of LMOD2 and TMOD4 are altered in LMOD3-NM.** (A) Western blot analysis of thin filament pointed end proteins LMOD2, TMOD1, and TMOD4 in patients with LMOD3-NM and age-matched controls. Coomassie-stained MHC, sarcomeric actin, GAPDH, and  $\alpha$ -actinin-2 served as loading controls. (B) Histograms show normalized protein levels for TMOD1, TMOD4, and LMOD2 in patients with LMOD3-NM and controls. TMOD1 expression levels are variable in both patients and controls, with no consistent difference between these groups. TMOD4 levels are consistently reduced in patients with LMOD3-NM compared with age-matched controls. LMOD2 expression is upregulated in patients. Densitometry was performed using ImageJ, and values were normalized to  $\alpha$ -actinin-2 levels and are scaled to mean control level = 1.0. Patients with low or no expression of muscle proteins were excluded from analysis (e.g., patient 4). Dotted lines show the average results for patients and controls, respectively.

rare genetic disorders, delivering accurate genetic counselling for families, permitting prenatal diagnosis, and facilitating studies of disease pathogenesis and treatment.

## Methods

### Gene identification and genetic screening

WES was performed in 2 siblings with NM and their unaffected non-consanguineous parents (family 14 in Table 1), as described previously (21). Exome variant filtering for Mendelian disease gene discovery focused on genes containing homozygous or compound heterozygous variants (21). The Broad Institute whole-exome data set can be found in the database of Genotypes and Phenotypes site (<http://www.ncbi.nlm.nih.gov/gap>; accession no. phs000655.v1.p1). For more details, see the Supplemental Methods.

In family 1, candidate chromosomal loci were first identified by genetic mapping using Affymetrix 250K GeneChip microarrays and multipoint linkage analysis combined with homozygosity mapping.

This reduced the candidate regions to 3% of the genome. WES was then performed in the index case. WES was performed in a similar manner to that described for family 14. Exome libraries were captured using the Agilent SureSelect V3. SNPs and small indels were called using SAM tools and annotated using ANNOVAR. Homozygous single nucleotide variants mapping to candidate loci were filtered as described for family 14.

### Genetic screening for additional LMOD3 mutations

Bidirectional Sanger sequencing of LMOD3 was performed on bio-banked DNA in 476 additional genetically unresolved patients with NM in Helsinki, London, Perth, Sydney, and Tokyo. LMOD3 was PCR amplified from genomic DNA in 4 fragments covering 3 exons using standard methods (PCR primer sequences in Supplemental Table 3). An additional 68 cases were screened by WES or whole-genome sequencing in Boston through the Boston Children's Hospital Gene Partnership Program. WES in these cases was performed as previously described (3). In cases screened by whole-genome sequencing,

this was performed by Complete Genomics and processed through their Standard Pipeline v. 2.2.

### Abs

A polyclonal rabbit anti-LMOD3 Ab was purchased from Proteintech (14948-1-AP) and used at a dilution of 1:10,000 for Western blot and 1:350 for immunohistochemistry. Two polyclonal rabbit LMOD2 Abs (Abcam, 108022, and Santa Cruz, sc-135493, S-12) were used for Western blot at dilutions of 1:250 and 1:500, respectively. The specificity of LMOD2 and LMOD3 Abs was confirmed using recombinant proteins expressed in bacteria and COS cells (see Supplemental Figure 1). The rabbit  $\alpha$ -actinin-2 Ab (clone 4A3, 1:250,000 for Western blot) was developed in-house by A.H. Beggs. Mouse  $\alpha$ -actinin Ab was purchased from Sigma-Aldrich (EA-53, 1:400 immunohistochemistry). Total sarcomeric actin levels were assessed using a mouse sarcomeric actin Ab from Sigma-Aldrich (5C5, 1:10,000 for Western blot). The GAPDH Ab was obtained from Millipore (MAB374, 1:10,000 for Western blot). Developmental MHC Ab, which recognizes the embryonic MHC isoform, was purchased from Novocastra Laboratories Ltd (NCL-MHCd, dilution 1:200 for Western blot), cardiac actin Ab was purchased from American Research Product Inc. (1:1,500 for Western blot), slow MHC Ab was purchased from Chemicon International Inc. (MAB1628, dilution 1:3,000 Western blot, 1:1,000 immunohistochemistry), and fast MHC Ab was purchased from Sigma-Aldrich (MY-32, 1:800 immunohistochemistry). TMOD1 and TMOD4 Abs were produced in-house by V.M. Fowler (dilution for immunohistochemistry was 1:50 and 1:100 for TMOD4 and TMOD1, respectively; ref. 22). Secondary Abs (Alexa Fluor 555 rabbit and Alexa Fluor 647 mouse, 1:200) for immunohistochemistry were obtained from Molecular Probes, Invitrogen. HRP-conjugated secondary Abs for Western blot were purchased from GE Healthcare (1:2,000).

### Western blot

Western blotting methods for human samples and cells were based on methods previously described with modifications (23). Protein concentration was determined via bicinchoninic acid BCA assay per manufacturer's instructions (Pierce, Thermo Fisher Scientific). Five  $\mu$ g total muscle protein was separated on precast 10% SDS-PAGE gels (NuPAGE NovexBis-Tris Gels, Invitrogen, Life Technologies, or Bio-Rad) for the detection of LMOD3, followed by transfer of proteins onto nitrocellulose membrane for 1 hour in Tris-Glycine buffer containing 0.075% SDS. Membranes were blocked in 5% skim milk (diluted in PBS 0.1% Tween 20) for 1 hour, followed by incubation in primary Ab for 2 hours at room temperature or for 16 hours at 4°C. Unbound primary Ab was removed by washing for 25 minutes in PBS 0.1% Tween 20, followed by 15 minutes of blocking. Secondary HRP Ab (1:2,000 in block for 1 hour at room temperature) and ECL Chemiluminescence Detection System (GE Healthcare Life Science) were used for detection. In some cases membranes were stripped of bound Ab by washing in 62.5 mM Tris-HCl, pH 6.8, 2% SDS, and 0.1 M  $\beta$ -mercaptoethanol for 30 minutes. Stripping buffer was removed by washing 5 times for 1 minute in large volumes of PBS 0.1% Tween 20, and membranes were reprobed. Membranes were stained for total proteins with Coomassie Blue Brilliant (Sigma-Aldrich).

For Western blot studies of zebrafish samples, protein extracts were established from flash frozen fish embryo samples (3 days after fertilization) using a RIPA protein extraction buffer with complete

Mini Protease inhibitor (Roche) and a Dounce tissue homogenizer (Pierce Biotechnology). Approximately 60  $\mu$ g protein was loaded per sample, resolved by polyacrylamide gel electrophoresis on 10% gels, and transferred to polyvinylidene fluoride membrane. After blocking in PBS containing 0.1% Tween, 5% dried milk, and 3% BSA, the membrane was probed with LMOD3 Ab (1: 5,000, Proteintech) and TMOD1 and TMOD4 (1:1,000, see *Abs*), with an actin Ab (1:10,000, Sigma-Aldrich) as loading control. Secondary Abs were used at 1:5,000 (Bio-Rad), and blots were developed using electrochemiluminescence reagent (GE Biosciences).

### Immunohistochemistry to determine LMOD3 localization in control muscle samples

Control quadriceps muscle tissue from 5 healthy individuals was fixed in 3% paraformaldehyde in a stretched position, embedded in TissueTek, and frozen in 2-methylbutane cooled in liquid nitrogen. Longitudinal 8- $\mu$ m-thick cryosections were collected on glass slides and blocked for 1 hour in 4% BSA prepared in PBS, followed by incubation in primary Abs diluted in blocking solution for 2 hours at room temperature. Sections were labeled with rabbit LMOD3 Ab and slow MHC, fast MHC, or  $\alpha$ -actinin-2 Ab. Unbound Abs were removed by washing 4 times in PBS, followed by 15 minutes of blocking as above. Secondary anti-mouse Alexa Fluor 647, anti-rabbit Alexa Fluor 488, and Alexa Fluor 488-conjugated phalloidin (diluted 1:20, Life technology) were incubated on muscle sections for 1 hour. Finally, slides were washed as above and mounted using Immu-Mount (Thermo Scientific). Staining was imaged by confocal microscopy. Five areas were imaged per control biopsy, ensuring sarcomeres were adequately stretched, as determined by phalloidin staining. In each area imaged, the staining pattern was recorded (pointed end staining, staining along the thin filament, and combined pointed end and thin filament staining) and the fiber type was determined with MHC staining.

A subset of images showing high-quality pointed end LMOD3 staining were used to measure the distance from the Z-disc of the LMOD3 peak of intense staining. Measurements were first performed manually using ImageJ (profile blot function). Measurements were confirmed using Distributed Deconvolution Analysis (24).

### Tissue culture

Primary patient and control fibroblast cultures were transduced with a MyoD-lentiviral vector to induce myogenic conversion as described previously (4). Primary patient and control myoblasts and MyoD-converted fibroblasts were grown to confluency and differentiated in 5% horse serum with 1x ITS for 5 to 8 days to induce myotube formation. Western blot was performed using 5  $\mu$ g cell lysate from differentiated cells.

### *lmod3* MO zebrafish

Knockdown of *lmod3* gene expression in zebrafish was achieved by coinjection of morpholinos directed against the splice acceptor site of exon 2 and the splice donor site of exon 3. Morpholinos were injected at a concentration of 0.3 mM. Morpholino experiments were controlled by injecting an identical concentration and amount of standard control morpholino (GeneTools Inc.). All injections were done into 1-cell stage AB zebrafish embryos. All embryos were manually dechorionated at day 1 after fertilization. Histopathology, including immunofluorescence analysis of isolated myofibers and EM of muscle from whole embryos, was performed as previously described (25, 26).

**Assessment of muscle function.** Spontaneous coiling was assessed in zebrafish 24 hours after fertilization by counting the number of coiling events in a 15-second epoch. Groups of 20 live embryos were videoed together using a Nikon Macroscope, and then coiling was measured via examination of video data.

Touch-evoked escape response data was generated as previously described (27).

Contractile properties of whole zebrafish trunk muscles were measured at 3 days after fertilization as previously described (25, 28). The width of the trunk, as viewed from ventral and lateral aspects, was measured, and cross-sectional area was estimated from these measurements assuming an ellipse (28). Values are shown as mean  $\pm$  SD.

### Actin nucleation/polymerization assay

**Expression of recombinant leiomodins proteins.** Full-length LMOD2 and LMOD3 were expressed and purified as previously described (10). Following purification, proteins were exchanged into 20 mM Tris-HCl, pH 7.4, for biochemical assays.

**Actin purification.** Chicken pectoral skeletal muscle G-actin was purified from acetone powder as previously described (29) and was kept on ice in 2 mM Tris-HCl, pH 8, 0.5 mM DTT, 0.2 mM ATP, 0.2 mM CaCl<sub>2</sub>, 0.01% NaN<sub>3</sub> to use fresh in fluorescence experiments. Actin concentration was determined by measuring difference spectra in 6 M guanidine-HCl between pH 12.5 and 7.0, using extinction coefficients of 2,357 per tyrosine and 830 per tryptophan as previously described (30). G-actin labeled with pyrene-iodoacetamide was prepared as previously described (31). Labeling ratios (~90%) were calculated as previously described (32), and pyrene actin was stored in liquid nitrogen. Before experiments, pyrene actin was defrosted at 37°C and centrifuged at 386,000 g (TLA-100, Beckman) for 30 minutes at 4°C to remove aggregates. The same solution of G-actin was used for all experiments to decrease the measurement error.

**Fluorescence measurements.** Actin polymerization was monitored by the increase in fluorescence using a Photon Technology International spectrofluorometer, Model QM-40 (QuantaMaster-40) (excitation 366 nm and emission 387 nm, with a 2-nm slit). To measure actin nucleation by LMOD, 1.1  $\mu$ M G-actin (10% pyrenyl-actin) was mixed with 2, 5, 20, 50, and 100 nM LMOD, and the reaction was initiated by addition of 20x polymerization buffer to final concentrations of 10 mM imidazole, pH 7.0, containing 100 mM KCl, 2 mM MgCl<sub>2</sub>, and 1 mM EGTA. Spontaneous actin nucleation in the absence of LMOD was measured as a control.

### TM binding

**Peptides.** Peptides for CD measurements were synthesized by the Tufts University Core Facility. The TM peptide is a designed acetylated chimeric peptide that consists of 14 N-terminal residues of long  $\alpha$ -TM encoded by exon 1a, which contains the TMOD-binding site, and the 18 C-terminal residues of the GCN4 leucine zipper domain, which help to stabilize the coiled-coil structure (33, 34). Note that the corresponding N-terminal sequence of long muscle  $\beta$ -TM encoded by exon 1a is identical to the  $\alpha$ -TM sequence. Leiomodins fragments (amino acids 5–42 for mouse LMOD2 and amino acids 6–44 for mouse LMOD3) were designed based on alignment with the first TM-binding site of TMOD1. The synthetic peptides were purified and analyzed on HPLC, and their quality was confirmed using mass spectrometry. Concentrations of peptides were determined by a BCA Protein Assay Kit

(Pierce) and by measuring their difference spectra in 6 M guanidine-HCl as previously described (30).

**CD measurements.** CD measurements were done using an Aviv model 420SF spectrometer in 1-mm cuvettes. The peptide concentrations were 10  $\mu$ M in 100 mM NaCl, 10 mM Na-Phosphate buffer, pH 7.0. Change of helical content during temperature denaturation was monitored at 222 nm. The dissociation constants,  $K_D$ , of the LMOD/TM peptide complexes were determined as previously described (35). Dissociation constants were statistically compared using a 2-tailed *t* test, and values are shown as mean  $\pm$  SD.

### Single-fiber mechanics and staining of stretched myofiber bundles

Contractile properties were measured in myofiber bundles isolated from frozen muscle biopsies using methods described previously (16, 36). Force response to saturating Ca<sup>2+</sup> concentrations (pCa 4.5) was measured at different SLs 2.0, 2.2, 2.5, 2.8, 3.2, and 3.5  $\mu$ m. Forces were normalized to cross-sectional area measured at 2.5  $\mu$ m SL. For force/SL curves, forces at various SLs were normalized to the highest force obtained. At least 5 bundles were measured per biopsy. MHC isoform content of bundles was determined by SDS-PAGE electrophoresis as described previously (16). Force/SL curves were statistically compared with pooled control values using repeated-measures ANOVA. Values are shown as mean  $\pm$  SD.

For confocal imaging of phalloidin studies performed on myofiber bundles dissected from frozen LMOD3-NM patient biopsies and age-matched controls, small aluminum clips were glued to a glass slide. Fiber bundles from frozen biopsies were stretched and fixed between the aluminum clips in relaxing buffer with protease inhibitors. Stretched bundles were then fixed using 3% paraformaldehyde in PBS for 20 minutes at 4°C, followed by washes in PBS (5 buffer changes, last wash overnight at 4°C). Bundles were blocked for 1 hour in 1% BSA in PBS and labeled with 1 unit phalloidin conjugated to Alexa Fluor 488 for 48 hours. Unbound phalloidin was rinsed off, and bundles were mounted in Vectashield (Vector Laboratories) with #0 coverslips. Staining was analyzed by confocal microscopy, and thin filament length was measured using ImageJ (version 1.44, from Wayne Rasband, National Institutes of Health, Bethesda, Maryland, USA; <http://rsb.info.nih.gov/ij/index.html>).

### Statistics

Statistical analysis was performed as specified in figure legends and in the appropriate methods section. A *P* value of less than 0.05 was considered significant.

### Study approval

Ethical approval for this research was obtained from the Human Research Ethics Committees of the Children's Hospital at Westmead (10/CHW/45), the University of Western Australia, Bicêtre University Hospital (NI10054), the Children's Hospital of the University of Helsinki, the Japanese National Center of Neurology and Psychiatry, and the Boston Children's Hospital Institutional Review Board (03-08-128R). Written informed consent was obtained for genetic testing of participants, biobanking of patient muscle and DNA, and publishing of patient photographs. Mouse muscle analyses were performed using an Animal Care and Ethics Committee protocol locally approved at the Children's Hospital at Westmead. Zebrafish were housed and bred under the University of Michigan's University Com-

mittee on the Use and Care of Animal-approved conditions, and all experiments were done via a protocol approved by the ethics board of the University of Michigan.

## Acknowledgments

This work was funded by the National Health and Medical Research Council of Australia (1022707 and 1031893 to N.F. Clarke, K.N. North, and N.G. Laing; 1035828 to N.F. Clarke; 1035955 to G. Ravenscroft; 0511981 to K.G. Quinlan; 1002147 to N.G. Laing; and 1075451 to S.A. Sandaradura), the Association Française contre les Myopathies (15734 to G. Ravenscroft and N.G. Laing; DAJ1891 to J. Melki), the National Hospital Clinical Research Program (AOM10181 to J. Melki), the National Institute of Child Health and Development of the NIH (R01 HD075802 to A.H. Beggs), the Muscular Dystrophy Association (USA) (MDA201302 to A.H. Beggs), the AUism Charitable Foundation (to A.H. Beggs), and the National Institute on Aging (AG000114 to D.D. Sloboda). M. Kreissl is supported by a University of Sydney Australian Postgraduate Award and an International Postgraduate Research Scholarship. E.J. Todd is supported by a University of Western Australia Postgraduate Award. O. Ceyhan-Birsoy is supported by a Dubai-Harvard Foundation for Medical Research postdoctoral fellowship and Schlumberger Foundation Faculty for the Future grant. A. D'Amico and E. Bertini are supported by the Italian Ministry of Health Ricerca finalizzata (GR-2010-2310981). A.S. Kostyukova is supported by NIH grant GM081688, and V.A. Gupta is supported by NIH grant K01 AR062601. D.S. Gokhin is supported by a Development Grant from the Muscular Dystrophy Association (USA). Exome sequencing was supported by grants from the National Human Genome Research

Institute of the NIH (Medical Sequencing Program grant U54 HG003067 to the Broad Institute principal investigator, Lander) and by the Gene Partnership Project of Boston Children's Hospital. The authors would like to thank the study patients and their families, without whose participation this work would not have been possible. We thank F. Muntoni (Dubowitz Neuromuscular Centre, UCL Institute of Child Health and Great Ormond Street Hospital for Children), C. Lacroix, (Service de Neuropathologie, CHU Bicêtre), V. Zupan-Simunek (Service de Neonatologie, Hôpital Antoine Bécélère), A. Kan and N. Graf (The Children's Hospital at Westmead), and F. Fattori (Bambino Gesù Children's Hospital) for contribution and/or analysis of patient samples; S. Brammah (Concord Hospital) for provision of EM control images; T. Peduto (The Children's Hospital at Westmead) for assistance with analysis of muscle MRI; D.M. Margulies (Boston Children's Hospital) for support of WES through The Gene Partnership; and T. Yu and P. Park (Boston Children's Hospital) for WES pipeline development. We thank S.V. Brooks (University of Michigan) for assistance with experimental work and R. Dominguez (University of Pennsylvania) for providing reagents.

Address correspondence to: Kathryn N. North, Murdoch Children's Research Institute, The Royal Children's Hospital, Flemington Road, Parkville, VIC 3052, Australia. Phone: 61.3.83416226; E-mail: kathryn.north@mcri.edu.au.

Nigel G. Laing, Gianina Ravenscroft, Emily J. Todd's present address is: Harry Perkins Institute of Medical Research and Centre for Medical Research, University of Western Australia, Nedlands, Western Australia, Australia.

- North KN, Laing NG, Wallgren-Pettersson C. Nemaline myopathy: current concepts. The ENMC International Consortium and Nemaline Myopathy. *J Med Genet.* 1997;34(9):705-713.
- Romero NB, Sandaradura SA, Clarke NF. Recent advances in nemaline myopathy. *Curr Opin Neurol.* 2013;26(5):519-526.
- Gupta VA, et al. Identification of KLHL41 mutations implicates BTB-Kelch-mediated ubiquitination as an alternate pathway to myofibrillar disruption in nemaline myopathy. *Am J Hum Genet.* 2013;93(6):1108-1117.
- Cooper ST, et al. Dystrophinopathy carrier determination and detection of protein deficiencies in muscular dystrophy using lentiviral MyoD-forced myogenesis. *Neuromuscul Disord.* 2007;17(4):276-284.
- Lattanzi L, et al. High efficiency myogenic conversion of human fibroblasts by adenoviral vector-mediated MyoD gene transfer. An alternative strategy for ex vivo gene therapy of primary myopathies. *J Clin Invest.* 1998;101(10):2119-2128.
- Nanda V, Miano JM. Leiomodulin 1, a new serum response factor-dependent target gene expressed preferentially in differentiated smooth muscle cells. *J Biol Chem.* 2011;287(4):2459-2467.
- Conley CA, Fritz-Six KL, Almenar-Queralt A, Fowler VM. Leiomodins: larger members of the tropomodulin (Tmod) gene family. *Genomics.* 2001;73(2):127-139.
- Castillo A, Nowak R, Littlefield KP, Fowler VM, Littlefield RS. A nebulin ruler does not dictate thin filament lengths. *Biophys J.* 2009;96(5):1856-1865.
- Gokhin DS, Kim NE, Lewis SA, Hoenecke HR, D'Lima DD, Fowler VM. Thin-filament length correlates with fiber type in human skeletal muscle. *Am J Physiol Cell Physiol.* 2012;302(3):C555-C565.
- Chereau D, et al. Leiomodulin is an actin filament nucleator in muscle cells. *Science.* 2008;320(5873):239-243.
- Skwarek-Maruszewska A, et al. Different localizations and cellular behaviors of leiomodulin and tropomodulin in mature cardiomyocyte sarcomeres. *Mol Biol Cell.* 2010;21(19):3352-3361.
- Tsakada T, Pappas CT, Moroz N, Antin PB, Kostyukova AS, Gregorio CC. Leiomodulin-2 is an antagonist of tropomodulin-1 at the pointed end of the thin filaments in cardiac muscle. *J Cell Sci.* 2010;123(pt 18):3136-3145.
- Granzier HL, Akster HA, Ter Keurs HE. Effect of thin filament length on the force-sarcomere length relation of skeletal muscle. *Am J Physiol.* 1991;260(5):C1060-C1070.
- Ryan MM, et al. Nemaline myopathy: a clinical study of 143 cases. *Ann Neurol.* 2001;50(3):312-320.
- Witt CC, et al. Nebulin regulates thin filament length, contractility, and Z-disk structure in vivo. *EMBO J.* 2006;25(16):3843-3855.
- Ottenheim CAC, Witt CC, Stienen GJ, Labeit S, Beggs AH, Granzier H. Thin filament length dysregulation contributes to muscle weakness in nemaline myopathy patients with nebulin deficiency. *Hum Mol Genet.* 2009;18(13):2359-2369.
- Agrawal PB, et al. Heterogeneity of nemaline myopathy cases with skeletal muscle alpha-actin gene mutations. *Ann Neurol.* 2004;56(1):86-96.
- Nowak KJ, et al. Nemaline myopathy caused by absence of  $\alpha$ -skeletal muscle actin. *Ann Neurol.* 2007;61(2):175-184.
- Ravenscroft G, et al. Mutations in KLHL40 are a frequent cause of severe autosomal-recessive nemaline myopathy. *Am J Hum Genet.* 2013;93(1):6-18.
- Garg A, et al. KLHL40 deficiency destabilizes thin filament proteins and promotes nemaline myopathy. *J Clin Invest.* 2014;124(8):3529-3539.
- Menezes MP, et al. Whole exome sequencing identifies three recessive FIG4 mutations in an apparently dominant pedigree with Charcot-Marie-Tooth disease. *Neuromuscul Disord.* 2014;24(8):666-670.
- Gokhin DS, et al. Tropomodulin isoforms regulate thin filament pointed-end capping and skeletal muscle physiology. *J Cell Biol.* 2010;189(1):95-109.
- Cooper ST, Lo HP, North KN. Single section Western blot: improving the molecular diagnosis of the muscular dystrophies. *Neurology.*

- 2003;61(1):93–97.
24. Littlefield R, Fowler VM. Measurement of thin filament lengths by distributed deconvolution analysis of fluorescence images. *Biophys J*. 2002;82(5):2548–2564.
25. Telfer WR, Nelson DD, Waugh T, Brooks SV, Dowling JJ. Neb: a zebrafish model of nemaline myopathy due to nebulin mutation. *Dis Model Mech*. 2012;5(3):389–396.
26. Majczenko K, et al. Dominant mutation of CCDC78 in a unique congenital myopathy with prominent internal nuclei and atypical cores. *Am J Hum Genet*. 2012;91(2):365–371.
27. Telfer WR, Busta AS, Bonnemann CG, Feldman EL, Dowling JJ. Zebrafish models of collagen VI-related myopathies. *Hum Mol Genet*. 2010;19(12):2433–2444.
28. Sloboda DD, Clafin DR, Dowling JJ, Brooks SV. Force measurement during contraction to assess muscle function in zebrafish larvae. *J Vis Exp*. 2013;(77). doi:10.3791/50539.
29. Kostyukova AS, Hitchcock-DeGregori SE. Effect of the structure of the N terminus of tropomyosin on tropomodulin function. *J Biol Chem*. 2004;279(7):5066–5071.
30. Kostyukova AS, Hitchcock-DeGregori SE, Greenfield NJ. Molecular basis of tropomyosin binding to tropomodulin, an actin-capping protein. *J Mol Biol*. 2007;372(3):608–618.
31. Kouyama T, Mihashi K. Fluorimetry study of N-(1-pyrenyl)iodoacetamide-labelled F-actin. Local structural change of actin protomer both on polymerization and on binding of heavy meromyosin. *Eur J Biochem*. 1981;114(1):33–38.
32. Cooper JA, Walker SB, Pollard TD. Pyrene actin: documentation of the validity of a sensitive assay for actin polymerization. *J Muscle Res Cell Motil*. 1983;4(2):253–262.
33. Greenfield NJ, Montelione GT, Farid RS, Hitchcock-DeGregori SE. The structure of the N-terminus of striated muscle alpha-tropomyosin in a chimeric peptide: nuclear magnetic resonance structure and circular dichroism studies. *Biochemistry*. 1998;37(21):7834–7843.
34. Greenfield NJ, Palm T, Hitchcock-DeGregori SE. Structure and interactions of the carboxyl terminus of striated muscle alpha-tropomyosin: it is important to be flexible. *Biophys J*. 2002;83(5):2754–2766.
35. Kostyukova AS. Leiomodlin/tropomyosin interactions are isoform specific. *Arch Biochem Biophys*. 2007;465(1):227–230.
36. de Winter JM, et al. Troponin activator augments muscle force in nemaline myopathy patients with nebulin mutations. *J Med Genet*. 2013;50(6):383–392.
37. Zdobnov EM, Apweiler R. InterProScan — an integration platform for the signature-recognition methods in InterPro. *Bioinformatics*. 2001;17(9):847–848.